High-luminosity Large Hadron Collider with laser-cooled isoscalar ion beams

M.W. Krasny, A. Petrenko, W. Placzek

Version of Record: https://www.sciencedirect.com/science/article/pii/S0146641020300399
Manuscript_5dfe33bbdefe82c8ab36380e00b4546e

High-luminosity Large Hadron Collider with laser-cooled isoscalar ion beams †

M. W. Krasny [a,b], **A. Petrenko** [c,b] *and* **W. Płaczek** [d]

[a] *LPNHE, Sorbonne Université, Université de Paris, CNRS/IN2P3, Tour 33, RdC, 4, pl. Jussieu, 75005 Paris, France*
[b] *CERN, Geneva, Switzerland*
[c] *Budker Institute of Nuclear Physics, Prospekt Akademika Lavrent'yeva 11, Novosibirsk, Russia*
[d] *Institute of Applied Computer Science, Jagiellonian University, ul. Łojasiewicza 11, 30-348 Krakow, Poland*

Abstract

The existing CERN accelerator infrastructure is world unique and its research capacity should be fully exploited. In the coming decade its principal *modus operandi* will be focused on producing intense proton beams, accelerating and colliding them at the Large Hadron Collider (LHC) with the highest achievable luminosity. This activity should, in our view, be complemented by new initiatives and their feasibility studies targeted on re-using the existing CERN accelerator complex in novel ways that were not conceived when the machines were designed. They should provide attractive, ready-to-implement research options for the forthcoming *paradigm-shift* phase of the CERN research. This paper presents one of the case studies of the *Gamma Factory* initiative [1] – a proposal of a new operation scheme of ion beams in the CERN accelerator complex. Its goal is to extend the scope and precision of the LHC-based research by complementing the proton–proton collision programme with the *high-luminosity* nucleus–nucleus one. Its numerous physics highlights include studies of the exclusive Higgs-boson production in photon–photon collisions and precision measurements of the electroweak (EW) parameters. There are two principal ways to increase the LHC luminosity which do not require an upgrade of the CERN injectors: (1) modification of the beam-collision optics and (2) reduction of the transverse emittance of the colliding beams. The former scheme is employed by the ongoing high-luminosity (HL-LHC) project. The latter one, applicable only to ion beams, is proposed in this paper. It is based on laser cooling of bunches of partially stripped ions at the SPS flat-top energy. For isoscalar calcium beams, which fulfil the present beam-operation constrains and which are particularly attractive for the EW physics, the transverse beam emittance can be reduced by a factor of 5 within the 8 seconds long cooling phase. The predicted nucleon–nucleon luminosity of $L_{NN} = 4.2 \times 10^{34}\,\mathrm{s}^{-1}\mathrm{cm}^{-2}$ for collisions of the cooled calcium beams at the LHC top energy is comparable to the levelled luminosity for the HL-LHC proton–proton collisions, but with reduced pile-up background. The scheme proposed in this paper, if confirmed by the future Gamma Factory proof-of-principle experiment, could be implemented at CERN with minor infrastructure investments.

† This paper is dedicated to the memory of Evgeny Bessonov, the Gamma Factory group member and our colleague, who passed away recently.

Contents

1 Introduction

The Large Hadron Collider (LHC) is a collider of partonic bunches containing a dynamical mixture of quarks, gluons and photons. The partonic bunch carriers which guarantee their stability over the beam acceleration and storage time are protons and stable nuclei (ions) characterised by their proton, Z, and neutron, $A - Z$, content, where A is the mass number of the nucleus.

The use of the ion beams at the LHC has, so far, been largely confined to studies of the strong-interaction phenomena. The precision studies of the Standard Model (SM) electroweak (EW) interactions and searches for new, beyond the Standard Model (BSM), processes have been carried out using the proton beams. There were three obvious reasons for that.

The first one was extending the collision energy of colliding partons to its maximal value, specified by the maximal magnetic field of the LHC dipoles – partons carried by protons have their maximal energies larger by at least a factor of two than those carried by nuclei at the same parent-beam-particle magnetic rigidity.

The second was minimising the multiplicity of background particles obscuring the detection and measurement of the SM EW and BSM partonic processes. These background particles are produced in ordinary, strong-interactions mediated, collisions of spectator partons which accompany partons taking part in the SM EW or BSM processes of interest. For the low luminosity LHC, characterised by a negligible multi-collision pile-up, the number of parasitic collisions of spectator partons grows quickly with the nuclear mass number A of colliding particles. It is minimal for the proton–proton (pp) collisions.

The third and the most constraining reason was maximising the partonic-collision luminosity to look for very rare BSM processes and reducing statistical errors of the SM EW measurements. At the LHC, the number of partons transported to their collision point in nuclear envelopes is significantly smaller than the number of partons transported by protons. This is due to several Z-dependent beam intensity-limiting effects, such as: the achievable yields of beam particles coming from the proton and ion sources, space-charge and intra-beam scattering effects in bunched beams, and – for the large-Z ions – the presence of parasitic beam-burning processes affecting the beam safety in the superconducting rings.

For the above three reasons the pp collision scheme has always been assumed to be superior with respect to the nucleus–nucleus (AA) one.

In this paper we argue that – in the forthcoming high-luminosity (HL) phase of the LHC experimental programme – the above arguments in favour of the use of the proton beams for the studies of the SM EW and BSM phenomena lose their strength, or can be circumvented by introducing a new operation scheme of ion beams which includes reduction of their transverse emittance by laser-cooling.

In order to find the optimal balance for the LHC research programs based on the proton and nuclear partonic bunches the following question have to be addressed:

- What are the advantages of nuclei for which the u and d valence-quark, photon and gluon composition can be tuned to their physics-goal-optimised values?

- What is the optimal beam-particle choice which maximises the rate of SM EW and BSM partonic collisions with respect to the beam-burning parasitic collisions?
- What is the optimal beam-particle choice which minimises the multi-collision pile-up background for the LHC bunched beams at the highest partonic luminosity?
- Which partonic bunch carrier maximises the effective rate of photon–photon collisions?
- Which beam particle allows for the most precise experimental control of the flavour-dependent fluxes and effective emittances of its quarks, antiquarks and gluons?

The analysis presented in the first part of this paper leads to the conclusion that the isoscalar, $Z = A/2$, nuclei – so far not considered as attractive partonic bunch carriers – have numerous advantages with respect to protons in the high-luminosity phase of the LHC research programme, in particular for the precision measurements of the SM EW parameters and for the detailed experimental investigation of the EW symmetry-breaking mechanism.

From the historical perspective, such a conclusion is not original, as the progress in understanding the weak-interaction sector of SM in the 1970s, 1980s and 1990s was made by studying lepton scattering on isoscalar nuclei rather than hydrogen targets: (1) iron (Fe)[1] in the CDHS experiment at CERN [2], CCFR experiment at FNAL [3], NuTeV experiment at FNAL [4], E140 experiment at SLAC [5]; and (2) calcium (Ca) in the CHARM experiment at CERN [6]. Special runs were proposed at HERA at DESY with a deuterium beam [7] to resolve the light-flavour structure of a proton. Finally, a fixed-target muon–deuterium scattering experiment was proposed at the SPS [8], as a support experiment for the LHC precision-measurement programme. The goal of the latter two initiatives was to reduce the interpretation ambiguities of the SM EW measurements at the LHC.

The most likely reason for which the beams of isoscalar ions have never been considered as portal to precision studies of the SM EW and BSM phenomena at the LHC is that, so far, no scheme has been proposed to achieve high partonic luminosities in AA collisions – comparable to the ones for the proton beams.

In this paper we propose such a scheme. The underlying idea is to reorganise the electron-stripping sequence of the CERN ion beams in order to allow ions to carry a small number of attached electrons over their SPS acceleration cycle. The atomic degrees of freedom of the beam particles are used, in the proposed scheme, to cool the beam by laser photons at the top SPS energy, and reduce its transverse emittance. The beam-cooling phase, lasting a couple of seconds, is then followed by stripping the remaining electrons in the SPS-to-LHC transfer line. The small-transverse-emittance fully stripped ion beam is then accelerated and brought to collisions with the counter-propagating beam in the LHC interaction points.

[1]Fe has a small excess of neutrons over protons, so the corresponding non-isoscalarity correction had to be made.

The isoscalar calcium beam is chosen for a concrete implementation of the proposed scheme. It satisfies the numerous beam operation constraints, discussed in this paper, and maximises its physics potential – both in the EW and BSM sectors.

Longitudinal laser cooling of low-energy and low-intensity atomic beams in storage rings has already been demonstrated [9, 10]. The transverse laser cooling of such beams has been studied in [11]. The evaluation of various techniques of longitudinal and transverse cooling of atomic beams at ultra-relativistic energies will soon be addressed in the forthcoming R&D phase of the Gamma Factory studies [1, 12] – in its Proof-of-Principle (PoP) experiment [13]. If the Gamma Factory SPS PoP experiment confirms the simulation results presented in this paper and if the beam-cooling scheme is implemented, a path to high-luminosity operation of the LHC with nuclear beams will be wide open. Adding such a new LHC operation mode, as discussed in this paper, could extend the scope and improve the precision reach of the LHC scientific programme. The proposed scheme could pave a new way to achieving the ultimate partonic luminosity at the future hadronic colliders, such as the FCC.

This paper is organised as follows. In Section 2 we analyse the composition and properties of partonic bunches confined in protons and nuclei. In Section 3 we discuss the relative merits of proton and nuclear envelopes of partonic bunches for the LHC physics programme. In Section 4 we identify dominant luminosity-limiting factors for the AA collision scheme. Laser cooling of ultra-relativistic atomic beams is discussed in Section 5. It is followed, in Section 6, by the analysis of the beam operation constraints and the corresponding choice of the optimal beam particle species for their high-luminosity collisions at the LHC. Section 7 presents a proposal of a concrete implementation of the proposed scheme for the calcium beam. Finally, Section 8 contains conclusions and outlook. In Appendix B we discuss the technical aspects of kinematics and dynamics of photon absorption and emission by highly ionised atoms, relevant for this paper.

2 Protons and nuclei as carriers of partonic bunches

2.1 Space-time picture

Protons and nuclei colliding at the LHC, when "observed" in the rest-frame of the counter-propagating beam with high space-time resolution, can be considered as bunches of quasi-independent, point-like partons: quarks, gluons and photons. The principal difference of the bunches of these virtual partons and the classical bunches of protons is that the intra-bunch dynamics of the former is driven solely by the partonic-bunch-internal QCD and QED interactions. These interactions are by several orders of magnitude stronger than the intra-beam and extra-beam interactions of proton bunches. As a consequence, the emittance of partonic bunches is independent of the LHC-ring lattice and constant over the acceleration and storage cycle.

Each parton is confined within a fraction of the partonic-bunch space-time volume. This volume is fully determined by the energy, E_p, of the counter-propagating parton probing the inner structure of the partonic bunch, its energy-loss, ν, and momentum-loss,

q, in the space-time volume occupied by the parton. The principal difference of the proton and nuclear partonic bunches reflects their specific valence-quark, sea quark, gluon and photon composition as well as the A- and Z-dependent momentum distributions of their components.

The partonic distributions in the proton and nuclear bunches can be related to each other by simple formulae discussed in the subsequent sections. An extended discussion presenting the present status of the phenomenology of partonic distributions is presented in Appendix A.

2.2 Quarks

The flavour of partonic bunches is determined by the charge Z and atomic A numbers of their carriers. Protons contain two valence u quarks and one valence d quark. Nuclei contain $A+Z$ valence u quarks and $2A-Z$ valence d quarks. While the flavour composition of partonic bunches plays a very limited role in the strong interaction processes, it plays a central role in electromagnetic and weak processes. This is because u and d quarks carry different electric charges, $Q^{u,d}$, different weak isospin $t_{3L}^{u,d}$ and have different axial and vector couplings, $g_V^{u,d} = t_{3L}^{u,d} + 2Q^{u,d}\sin^2\theta_W$ and $g_A^{u,d} = t_{3L}^{u,d}$, to the EW Z-boson. As a consequence, the choice of the beam particle determines the beam-type-specific characteristics of collisions involving production of lepton pairs, W, Z and Higgs bosons.

The valence-quarks, together with their associated quark–antiquark sea pairs (of various flavours: up, down, strange, charm, bottom) and gluons, form – within the nuclear-bunch volume, defined by its radius $R_A = 1.2 \times A^{1/3}$ fm – clusters containing two valence u quarks and one valence d quark (virtual protons) and two valence d quarks and one valence u quark (virtual neutrons).

Since the binding energy of these virtual nucleons is significantly smaller than the nucleus mass, the distributions $u_v^{A,Z}(x_A, k_t, Q^2)$ and $d_v^{A,Z}(x_A, k_t, Q^2)$ of the fraction $x_A = p_q/p_A$ of the nuclear-partonic-bunch momentum carried by a valence-quark and of its transverse momentum k_t can be expressed at an arbitrary resolution scale $Q^2 = \nu^2 - q^2$ in terms of the corresponding distributions, $u_v^p(x_p, k_t, Q^2)$ and $d_v^p(x_p, k_t, Q^2)$, for unbound protons:

$$u_v^{A,Z}(x_A, k_t, Q^2) \approx (A - Z)d_v^p(x, k_t, Q^2) + Zu_v^p(x, k_t, Q^2) \tag{2.1}$$

and

$$d_v^{A,Z}(x_A, k_t, Q^2) \approx (A - Z)u_v^p(x, k_t, Q^2) + Zd_v^p(x, k_t, Q^2) \tag{2.2}$$

by setting $x_p = p_q/p_p = Ax_A = x$.

The corresponding momentum distributions of the u, d, s, c and b sea quarks and antiquarks, q_s, are also well approximated by

$$q_s^{A,Z}(x_A, k_t, Q^2) \approx Aq_s^p(x, k_t, Q^2). \tag{2.3}$$

Note that the isospin symmetry of the strong interactions implying: $u^p = d^n$ and $d^p = u^n$ has explicitly been used in the above formulae.

In reality, quark clusters are confined within the space-time volumes which are slightly larger than the volume of the free protons and neutrons and are surrounded by the nuclear-density-dependent virtual pion/kaon cloud. This meson cloud binds quark clusters within the nucleus volume. Finally, the quark clusters move within the nuclear bunch volume with the Fermi-motion velocities.

To account for the above nucleon binding effects, the quark and antiquark distributions in free protons, $q^p_{v,s}(x, k_t^2)$, have to be replaced in Eqs. (2.1), (2.2) and (2.3) by the modified distributions (see e.g. [14]):

$$q^{p/A}_{v,s}(x, k_t, Q^2) = R^A_{v,s}(x, k_t, Q^2) \times q^p_{v,s}(x, k_t, Q^2). \tag{2.4}$$

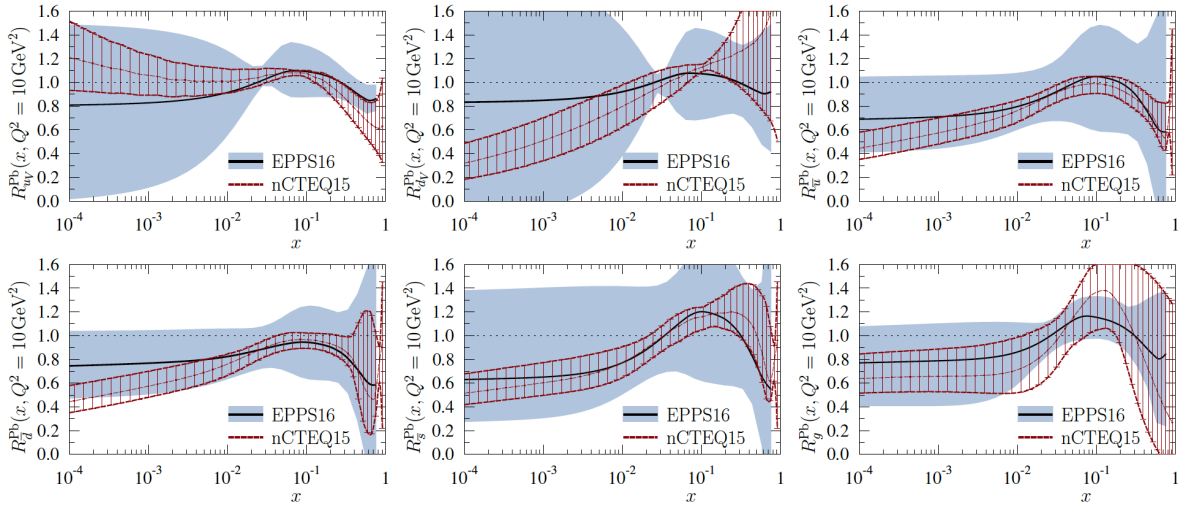

Figure 1: Nuclear modification factors for proton distribution functions of quarks and gluons, taken from [14].

The correction factors $R^A_{v,s}$ describe those of the strong interaction effects which cannot be controlled by the present perturbative computational methods of the theory of the strong interactions, the quantum chromodynamics (QCD), and must be measured. They quantify the approximations present in Eqs. (2.1), (2.2) and (2.3). It is important to note that the presence of the non-perturbative QCD correction factors does not modify the QCD evolution equations [15], providing a relationship of partonic distribution at a fixed and large resolution scale Q^2, except a very low x region (irrelevant to this paper). In Fig. 1 we recall their size, integrated over the transverse momentum of the partons, k_t, as extracted from the experimental data by the Eskola *et al.* [14] and CTEQ [16] groups. The correction factors do not differ significantly from 1 over the full range of the x-variable.

2.3 Photons

Nuclear partonic bunches carry a sizeable number of photons. Their photon content grows very fast with increasing charge of the nucleus, proportionally to Z^2. For the largest-Z

nuclei, photons are by a factor of $\sim 10^4$ more abundant than for the equivalent-energy protons. This property, specific to QED and absent in QCD, is confined to the kinematical regime in which the wavelength of the photon is larger than the nuclear bunch size. Such photons do not resolve the internal partonic-bunch structure and originate from a coherent action of all the charged constituents of partonic bunches. The coherence condition is fulfilled up to a maximum energy of the quasi-real photons of $\omega \leq \gamma_L/R_A$, where γ_L is the Lorentz factor of the beam particle and R_A is the radius of the nucleus. The transverse momentum of these photons satisfies the condition: $k_t \leq 1/R_A$. At higher photon energies, up to the maximum energy of $\omega \leq \gamma_L/R_N$, where R_N is the nucleon radius, the photon content of nuclear bunches is expected to rise proportionally to the beam-particle charge number Z. Finally, at still higher energies the photon content is expected to rise with increasing size of the nucleus proportionally to $A + Z/4$.

2.4 Gluons

Gluons are the most abundant constituents of the proton and nuclear bunches. Because of the colour confinement, gluons cannot propagate freely and are confined to the distances which are smaller than the nucleon diameter. Nuclear partonic bunch is a medium which does not conduct the colour current at the distances exceeding the nucleon size. As a consequence, the gluon content of the nuclear partonic bunches, contrary to the photon content, is not enhanced by the colour-charge coherence effects. It rises significantly slower with increasing size of the nucleus than the photon content.

The gluon momentum distributions for the nuclear bunches can be expressed in a similar way as the sea-quark distributions by the following expression:

$$G^A(x_A, k_t, Q^2) = A \times R_G^A(x, k_t, Q^2) \times G^p(x, k_t, Q^2). \tag{2.5}$$

It is important to note that since QCD is flavour-invariant, the gluon content of nuclear bunches rises proportionally to A and is independent of the electric charge Z of the nucleus.

In Fig. 1 the gluon nuclear modification factor R_G^A is presented in the lower-right corner. As expected, it is close to 1 and has a similar shape as the corresponding nuclear modification factors for the sea quarks.

3 Merits of proton and nuclear partonic bunches

3.1 High-energy frontier of partonic collisions

The equivalence of the fractional momenta distributions of the quarks and gluons in proton and nuclear bunches can be translated to the equivalence of their momentum distributions only if the following relation between the total momenta of the proton and nuclear bunches is fulfilled: $p_A = A \times p_p$. In reality, for the fixed beam magnetic rigidity, the maximal beam momentum of the nuclear beam is always lower by at least a factor of two than that of the proton beam: $p_A = (A \times p_p)/Z$.

There are two consequences of this constraint. They clearly demonstrate the unique merits of the proton partonic bunches at the LHC. Firstly, the high-energy frontier of partonic collisions, specified by the condition $x > 0.5$, is not accessible for collisions of nuclear bunches. Secondly, since the partonic momentum distribution decreases with increasing x, there will always be a penalty of smaller partonic luminosities for collisions of bound w.r.t. free nucleons (protons). The "penalty factors", defined as the ratio of partonic fluxes for the nuclear and proton bunches at the same beam magnetic rigidity, are sizeable in the region of $0.2 \leq x \leq 0.5$, in particular for collisions of gluons and sea quarks. They are small in the $x \approx 0.01$ region – the domain of interest for production of the W, Z and Higgs bosons at the LHC: in the range of 1.1–1.3 for u and d quarks, and in the range of 1.5–1.7 for the s, c, b quarks and gluons, at the resolution scale $Q^2 = M_Z^2$.

3.2 Precision frontier of partonic collisions

The interpretation of the measurements at the LHC requires a precise knowledge of the content and momentum distributions of partons in beam particles.

Proton partonic bunches appear to have an important advantage over the nuclear ones because the momentum distributions of partons in proton are, at present, known to higher precision. This is, to a large extent, related to the fact that the HERA collider – one of the principal sources of the information on partonic distributions – was running only in the electron–proton collision mode. The electron–nucleus collision mode was proposed in [17, 18]. It was developed initially as the DESY-internal project [19,20], and subsequently as a joint DESY-GSI project [21]. Following the DESY decision to choose, as the future HERA operation, mode the "high luminosity" electron–proton rather than electron–ion collisions, the project migrated to BNL and became the eRHIC project. The BNL-based electron–ion collider option was presented, for the first time, in [22]. Its physics and detector concepts, together with the accelerator requirements were developed further in [23–26]. The first eRHIC white paper was published in 2002 [27]. The project had to wait until the completion of the FRIB [28] construction to become, following extensive accelerator-design studies both at BNL and Jefferson Laboratory [29], the leading future accelerator-infrastructure project in the USA. One of its highlights is the precise measurement of the nuclear partonic distributions.

The present advantage of the proton bunches fades away in the high-luminosity, precision phase of the LHC experimental programme – in particular for the basic EW measurements, such as e.g. the measurements of the W-boson mass and $\sin^2\theta_W$. As argued in [30], the LHC restricted to its pp collision mode cannot improve their measurement precision that has already been achieved at the previous particle colliders. This is caused both by the limited statistics of the HERA charge-current as well as charm and beauty production events[2], and by the insufficient flavour-dependent constraints of partonic distributions coming from the analysis of the EW bosons and Drell–Yan lepton-pair pro-

[2]The proposed HERA upgrade programme included rebuilding of the injectors: Linac and DESY3. This investment was necessary to increase the HERA luminosity to a level that could have satisfied the LHC precision-programme requirements.

duction processes at the LHC[3]. While the precision of the LHC constraints will certainly improve with the increased statistics and development of more precise theoretical frameworks of the data analysis, no new experiments are planned to improve the precision of the necessary LHC-external constraints. Consequently, no matter what effort is made at the LHC, the precision of the several LHC key measurements will always be limited by the LHC-external data – as long as the proton–proton collisions remain the exclusive high-luminosity mode of the collider operation.

3.3 Isospin symmetry

The way to achieve the full, *in situ*, experimental control of the momentum distributions of partonic bunches at the LHC, proposed in this paper, is to exploit symmetries in the interactions of their constituents.

The proton bunches contain a mixture of u and d quarks which carry different electric charges $Q^{u,d}$ and different weak-isospin $t_{3L}^{u,d}$ components. Such bunches, as far as the EW processes are concerned, are equivalent to bunches containing a mixture of electrons and electron-neutrinos with their relative proportion known to a limited accuracy.

There is, however, an important difference in the above two cases. The pure electron and neutrino beams can be produced, while the pure beams of u and d quarks cannot. The solution proposed below is to choose their optimal and precisely controlled mixture. Such an optimal mixture is provided by the isoscalar, $Z = A/2$, nuclei for which – thanks to the isospin symmetry of the strong interactions – the momentum distributions of the u and d quarks are the same[4]:

$$u_{v,s}^{A=2Z,Z}(x, k_t, Q^2) = d_{v,s}^{A=2Z,Z}(x, k_t, Q^2). \tag{3.1}$$

Isoscalar-nuclei contain, like protons, a mixture of u and d quarks. What differs them from protons is that partonic momentum distributions, both in the valence and in the sea sectors and for all the Q^2 scales, become interrelated by the above symmetry relations.

Restoring the isospin symmetry of the first generation quarks can play a similar role in reduction of the LHC data interpretation ambiguities as exploiting the matter–antimatter symmetry for left–right symmetric detectors at the Tevatron collider. As we shall discuss in the next section, the isospin symmetry of isocalar nuclei allows to fully constrain the momentum distributions of the partonic bunches solely by the LHC data.

3.4 Flavour structure of isoscalar partonic bunches

At the LHC energies, the number of independent quark and antiquark momentum distribution functions describing proton and nuclear bunches (for five quark flavours: u, d,

[3]These processes do not suffer from uncertainties caused by an insufficient theoretical control of the hard-processes matrix elements and final-state interactions of quarks and gluons.

[4]A tiny violation of the equality may become important for ultra-high-precision measurements. The corresponding corrections, reflecting different electric charges of the u and d quarks, are however theoretically well controlled by QED.

s, c and b) is ten. The equality of the sea quark and antiquark distributions of the s, c, and b flavours, $s = \bar{s}$, $c = \bar{c}$ and $b = \bar{b}$, is a consequence of the gluonic-excitation origin of the heavy-flavour component of partonic bunches[5]. The above three constrains reduce the number of needed flavour-dependent distributions from ten to seven.

The measurements of momentum distributions of charged leptons in the Z, W^+, W^- and non-resonant lepton-pair production processes constrain five out of seven unknown quark flavour-dependent distributions[6], leaving the remaining two to be unconstrained. Note that for leptons produced at the Z-resonance peak, the distributions of both the negatively and positively charged lepton can be used.

For the proton bunches, the missing two constraints must be provided by the LHC-external data. The flavour content of the isoscalar partonic bunches is, on the contrary, fully constrained by the two isospin-symmetry relations (for the valence and sea quarks) expressed by the formula (3.1). Therefore, for the beams of isoscalar nuclei, the precision of the LHC measurements does not any longer depend upon the LHC-external constraints. Moreover, for the isoscalar nuclei, special observables can be defined [30], which facilitate the determination of specific partonic distributions. This is illustrated in the following example, discussed in details in [31].

Let us consider the W-boson charge asymmetry observable, $\mathrm{Asym}^{(+,-)}(p_{T,W})$ defined as:

$$\mathrm{Asym}^{(+,-)}(a) \;=\; \frac{d\,\sigma^+/d\,p_{T,W} - d\,\sigma^-/d\,p_{T,W}}{d\,\sigma^+/d\,p_{T,W} + d\,\sigma^-/d\,p_{T,W}}, \tag{3.2}$$

where $+$ and $-$ refer to the electric charge of the W boson, $d\,\sigma^{\pm}/d\,p_{T,W}$ is the differential cross section and $p_{T,W}$ is the transverse momentum of the W-boson. The asymmetry of the $p_{T,W}$ distribution reflects the flavour asymmetries in the distributions of transverse momentum k_t of quarks and antiquarks producing the W^+ and W^- bosons.

For the pp collision mode, as shown in the left-hand-side plot of Fig. 2, the expected asymmetry is significant. Its magnitude and shape are predominantly driven by the asymmetry in the transverse momentum, k_t, distributions of the u and d quarks. For the isoscalar beams, this dominant asymmetry source is suppressed and the remaining asymmetry is significantly reduced. It is driven essentially by the Cabibbo-suppressed difference of the respective distributions of the s and c quarks. The contribution of the b quarks is suppressed by the $|V_{ub}|^2$ element of the CKM matrix.

The right-hand-side plot in Fig. 2 illustrates the sensitivity of the W-boson charge asymmetry to the corresponding asymmetries in the transverse momentum distributions of the strange and charm quarks. Two extreme cases are shown, corresponding to $c = 0$

[5]For the s quarks, a small violation of this equality is likely and may call for a small correction to be applied; note that for the u and d quarks at $x \sim 6 \times 10^{-3}$ such an equality is violated at the level of $\sim$15% for protons.

[6]In the next-leading-order (NLO) QCD framework, the gluon momentum distribution influences as well the measured momentum distributions of produced leptons. This distribution is, however, constrained by the QCD evolution equations [15] which control the relationship between the quark (antiquark) and gluon distributions. The relation of the partonic distribution at the two resolution scales: $Q^2 = M_Z^2$ and $Q^2 = M_W^2$ is constrained by the dedicated measurement procedure discussed in details in [30].

and $c = s$, as an illustration of the $c - s$ constraining power of the W-boson charge asymmetry measured using the isoscalar nuclear beams.

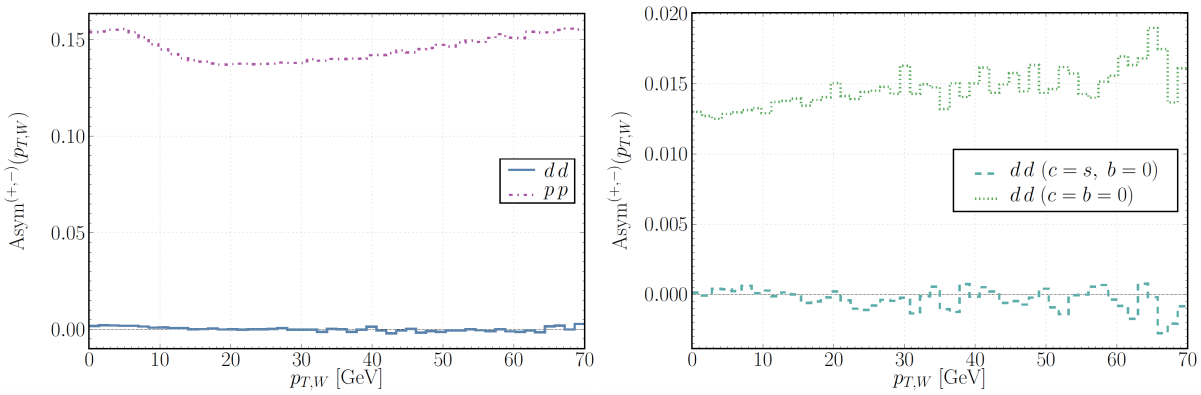

Figure 2: The predicted charge asymmetries of the transverse momentum of W-boson, $p_{T,W}$, for the isoscalar-nuclei (dd) and proton–proton (pp) collisions (LHS), and for the dd collisions under the following two assumptions: (1) $c = s$ and $b = 0$, and (2) $c = b = 0$ (RHS).

It remains to be added that in order to take the full profit from colliding the isoscalar bunches at the LHC, the statistical precision of the corresponding measurements must remain higher than the systematic one. This calls for the integrated nucleon–nucleon equivalent luminosity collected in such a running mode to exceed $100\,\mathrm{fb}^{-1}$ [30, 31].

3.5 New observables and measurement methods

Isoscalar nuclear beams allow to introduce new observables and new measurement methods which can be optimised to drastically reduce systematic errors and interpretation ambiguities of the LHC measurements. Such methods were at the heart of proposing in the 1990s, initially for the HERA physics programme and later adapted for the Tevatron physics programme, the concept of generic, model-independent analysis of the data collected at the high-energy colliders [32]. As an example of extension of such methods to the LHC environment, we present below the analysis strategy of asymmetries in inclusive charged-lepton distributions in the Z- and W-boson production processes.

Several subtle weak-interactions effects contribute to the asymmetries of the leptonic momenta distributions in the Z- and W-boson production processes. The charged-current (CC) coupling of quarks to the W-bosons is of the $V - A$ type, while their coupling to the Z-bosons is a coherent mixture of $V - A$ and $V + A$ couplings. This difference is reflected in the asymmetries in the angular distributions of leptons originating from the decays of the W and Z bosons. Radiative corrections affect differently the W and Z-boson production and decay amplitudes. While the effects of the QCD radiative corrections are driven mainly by the mass difference of the W and Z-bosons, the effects of the EW radiative corrections lead to several more subtle effects. First of all, the virtual EW corrections

affect differently the W and Z-boson absolute production rates. In addition, the radiation of photons affects differently the W and Z-boson propagation and decay. This is mainly driven by the differences in the interference pattern: (a) of the amplitudes for the photon emission from each of the charged leptons in Z-boson decays; (b) of the amplitudes of photon emission from the charged lepton and the charged W-boson.

The analysis strategy which amplifies the sensitivity to the above weak-interactions effects and drastically reduces the modelling uncertainties driven by the partonic distribution and strong-interactions effects was proposed in [33] and is recalled below.

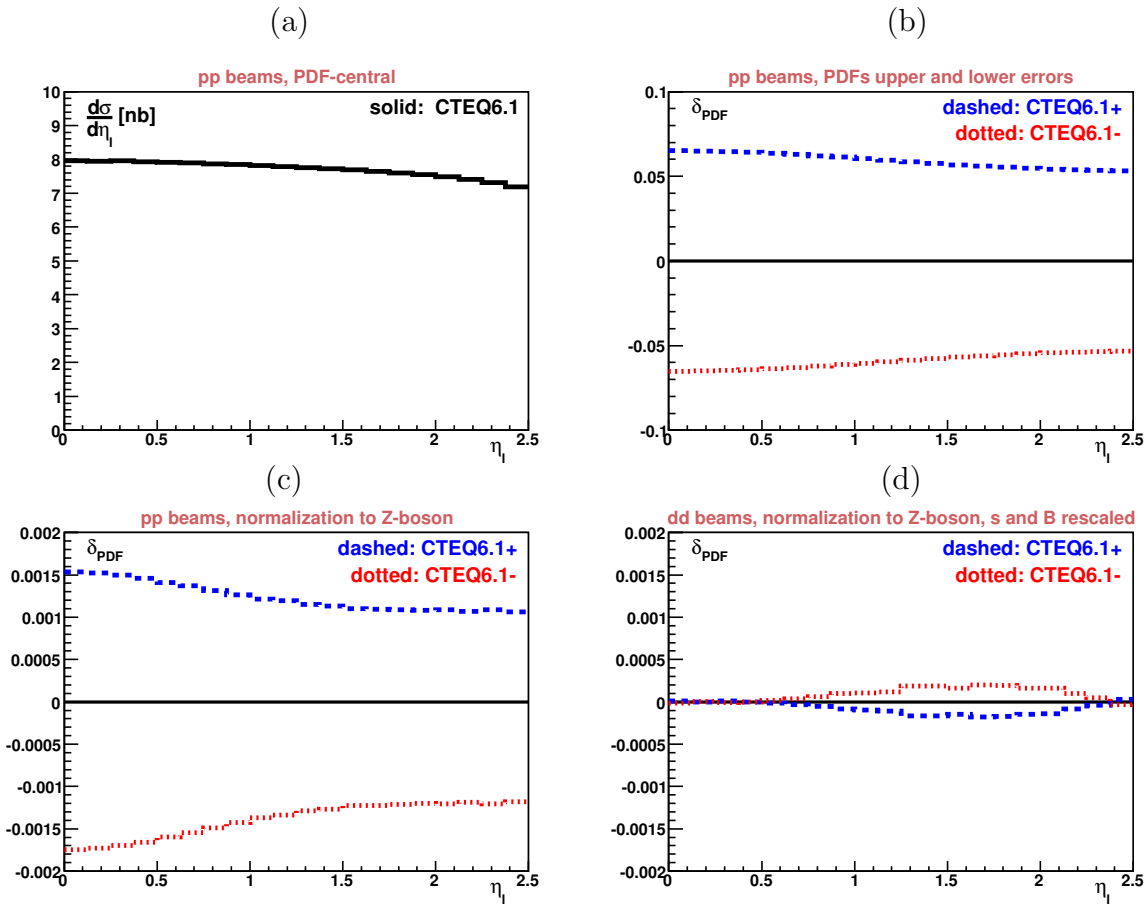

Figure 3: The distribution of the lepton pseudorapidity η_l for proton–proton collisions at LHC (a); the systematic uncertainty $\delta_{\rm PDF} = \frac{d\sigma/d\eta_l({\rm CTEQ6.1}\pm) - d\sigma/d\eta_l({\rm CTEQ6.1})}{d\sigma/d\eta_l({\rm CTEQ6.1})}$ of the η_l distribution reflecting the PDF uncertainty (b); as above but for the ratio of the η_l distributions for the W and Z-boson samples (c); as above but for the collision of the isoscalar beams, re-scaled collision energy, and re-scaled magnetic fields (see the text for details) (d).

In Fig. 3a we show the charged lepton pseudorapidity distribution for the $pp \to W+X$, $W \to l\nu$, process at the centre-of-mass (CM) energy of $\sqrt{s_n} = 14\,{\rm TeV}$ for the CTEQ6.1 parton distribution functions [34]. The dominant contribution to the uncertainty of this

distribution – coming from the uncertainties in the partonic distributions and determined using the method proposed in [35] – is shown in Fig. 3b. The partonic distributions related uncertainty can be diminished to the per-mil level by using, as an observable, the ratio of the charged lepton pseudorapidity distributions for the W and Z-boson production events. This uncertainty is shown in Fig. 3c.

Further reduction of the impact of the uncertainty of the partonic distribution functions can be achieved by replacing the proton collisions by the isoscalar-nucleus collisions and by measuring a new observable constructed using the measurements made at the following two colliding beam energy settings: $\sqrt{s_1}$ and $\sqrt{s_2} = (M_Z/M_W) \times \sqrt{s_1}$. These two settings allow to keep the momentum fractions of the partons producing Z and W-bosons equal if the W-boson sample is collected at the CM-energy $\sqrt{s_1}$ and the Z-boson sample at the CM-energy $\sqrt{s_2}$.

This new observable is defined as

$$R^{\rm iso}_{WZ} = \frac{d\sigma^{\rm iso}_W(s_1)}{d\sigma^{\rm iso}_Z(s_2)}\,. \tag{3.3}$$

It fully preserves the sensitivity to the EW effects. This observable is plotted in Fig. 3d as a function of the lepton pseudorapidity. Its sensitivity to the uncertainty in the partonic distribution functions is reduced[7] by more than two orders of magnitude, from the level of 5×10^{-2} to the level below 2×10^{-4}.

This example and the one discussed in the previous section show that the merits of the isoscalar partonic bunches may be exploited in two complementary ways:

- by fully constraining the flavour-dependent partonic distributions, as discussed in Section 3.4,
- by making these partonic distributions irrelevant for specially designed observables which amplify the EW effects w.r.t. the QCD ones, as discussed above.

3.6 Measurement of Standard Model parameters

The new observables and measurement methods, specially designed for the collisions of isoscalar partonic bunches, open the path to high-precision measurements of the SM EW parameters, such as the masses of the Z and W bosons, M_Z and M_W, and the weak-mixing angle (also called the Weinberg angle) θ_W. In SM they are inter-related by the tree-level expression[8]

$$\sin^2\theta_W = 1 - \frac{M_W^2}{M_Z^2}\,. \tag{3.4}$$

Out of the above three parameters, M_Z is known experimentally to a much better precision than the other two [36].

[7]Note that the nuclear effects which may affect differently u and d and quarks and the QCD-scale effects do not affect the observable defined above.

[8]This relation holds to the infinite perturbative order in the on-shell renormalisation scheme.

In practice, at both electron–positron and hadron–hadron colliders, instead of $\sin^2\theta_W$, the sine-squared of the so-called effective fermion mixing angle $\sin^2\theta^f_{\rm eff}$ is measured. It is related to the ratio of the vector to axial couplings of a given fermion f to the Z-boson and can be expressed as (see e.g. [37]):

$$\sin^2\theta^f_{\rm eff} = \kappa_f \sin^2\theta_W, \tag{3.5}$$

where the factors κ_f account for quantum-loop corrections, in particular those corresponding to the virtual top-quark and Higgs-boson contributions. Prior to the Higgs-boson discovery, the above relations were used for indirect determination of the SM Higgs mass. Now, when the Higgs-boson mass was measured, SM became over-constrained, and the relations (3.4) and (3.5) can be used for a consistency check of SM and a stringent test of various BSM scenarios. For example, the $\sin^2\theta^f_{\rm eff}$ measurement can be used as an indirect determination of the W-boson mass M_W, which should be consistent with its direcly measured value.

The LHC precision goal for the direct M_W measurement is $\sim 5\,\text{MeV}$. In order to achieve a comparable precision for an indirect determination, $\sin^2\theta^f_{\rm eff}$ should be measured with the precision of $\sim 10^{-4}$. The most precise up-to-date measurement was done by the LEP/SLD experiments for the leptonic $\sin^2\theta^l_{\rm eff}$, with the total error of 1.6×10^{-4} [38], which is equivalent to the indirect M_W-determination error of 8 MeV. The $\sin^2\theta^l_{\rm eff}$ value has also been measured at the LHC by the ATLAS [39], CMS [40] and LHCb [41] experiments with the precision of 3.6×10^{-4}, 5.3×10^{-4} and 10.6×10^{-4}, respectively. The ultimate goal of these experiments is to improve the precision of the LEP/SLD measurements.

The perspectives set up for the HL-LHC pp operation phase by the three experiments [42–44] are rather pessimistic: the final errors of the $\sin^2\theta^l_{\rm eff}$ measurements will be dominated by the uncertainties of the momentum distributions of partons – the corresponding errors are expected to be, at least, by a factor of 2–3 larger than the statistical errors.

The observable that is commonly used in experiments with unpolarised beams, both at the lepton and hadron colliders, to extract $\sin^2\theta^l_{\rm eff}$ is the forward–backward asymmetry in the process of the charged lepton-pair production (e^+e^- and/or $\mu^+\mu^-$) near the Z-boson peak:

$$A_{\rm FB} = \frac{\sigma_{\rm F} - \sigma_{\rm B}}{\sigma_{\rm F} + \sigma_{\rm B}}\,, \tag{3.6}$$

where $\sigma_{\rm F}$ and $\sigma_{\rm B}$ are the cross sections in the forward and backward hemispheres. The forward (backward) hemisphere is defined by the direction of motion of the incoming point-like fermions (antifermions): electrons (positrons) at e^+e^- colliders and quarks (antiquarks) at hadron colliders.

Contrary to the e^+e^- collisions where the incoming electron direction is known, for collisions of partonic bunches the incoming quark direction cannot be directly determined on an event-by-event basis. The LHC experiments rely on statistical correlations of this direction with the direction of the Lorentz boost of the outgoing lepton-pair[9], which is

[9]The valence quarks carry on average a higher momentum fraction than sea antiquarks.

used to define the forward–backward hemispheres on the event-by-event basis and, in turn, the asymmetry $A_{\rm FB}$ [40].

At the LHC energy, contrary to the Tevatron case, this observable suffers from the antiquark dilution corrections [40], requiring a very precise knowledge of the ratio of the quark and antiquark momentum distributions. Moreover, since the u and d quarks have different couplings to the Z-boson, they contribute with different weights to $A_{\rm FB}$. As a consequence, in the case of the proton partonic bunches for which $u_v \neq d_v$, the $A_{\rm FB}$ observable is highly sensitive to the difference in the momentum distributions of the valence u and d quarks[10].

For isoscalar partonic bunches the fractions of the valence u and d quarks are equal, cf. Eq. (3.1), and, as a consequence, the $A_{\rm FB}$ measurement no longer suffers from the limited precision of the $u_v - d_v$ distribution, which drives the measurement uncertainty for the proton bunches. In addition, the ratio of the quark to antiquark momentum distributions can be fully constrained by using the the observables and methods described in the previous subsection.

With the integrated luminosity of $3000\,{\rm fb}^{-1}$ from the HL-LHC pp-collision phase, the CMS and ATLAS experiments expect to reach the statistical errors of the $\sin^2\theta^l_{\rm eff}$ measurement at the level of 3–4×10^{-5} [42, 43], which is, at least, by a factor of ~ 4 smaller than the uncertainty related to the limited knowledge of partonic momentum distributions of proton bunches. For the collisions of isoscalar nucleus bunches, the latter uncertainty is reduced to a level at which the statistical errors become dominant. For the integrated nucleon–nucleon luminosity of $\sim 800\,{\rm fb}^{-1}$ collected in the isoscalar nucleus collision mode one would be able to reach the overall precision better than $\sim 10^{-4}$ for the $\sin^2\theta^l_{\rm eff}$ measurement per experiment.

For the direct W-boson mass measurement, the LHC experiments set an ambitious goal of reaching the precision of 5 MeV, or better. Up to date, only the ATLAS experiment has published its first result, with the total M_W error of 19 MeV, from the 2011 LHC run at the centre-of-mass energy of 7 TeV for the integrated luminosity of $4.6\,{\rm fb}^{-1}$ [45]. Two observables were used in this measurement: (1) the outgoing charged-lepton transverse momentum p_T^l, and (2) the W-boson transverse mass m_T. The p_T^l-based method is, in our view, the only method allowing to reach the precision $\delta M_W < 10\,{\rm MeV}$ at the LHC[11]. For this method, a considerable contribution to the total error of the ATLAS measurement comes from modelling of partonic distributions and QCD effects. The authors of [45] estimate this error to be 11.6 MeV, out of which about 70% results from the partonic distribution uncertainties. These estimates are, in our opinion, rather optimistic[12].

The studies presented in Refs. [30, 31] show that by replacing the proton beams by the isoscalar-nuclei beams one could drastically reduce the above modelling uncertainties. Even for rather conservative assumptions on the partonic distributions uncertainties in the

[10] One of us (MWK) is indebted to Arie Bodek for the in-depth discussions of the precision brick-walls in measuring $\sin^2\theta_W$ at high-energy hadronic colliders and on the possible ways to overcome them.

[11] For the m_T-based method, the uncertainty due to the missing recoil cannot, in our view, be reduced to a requisite level.

[12] For the detailed discussion of this aspect see e.g. [30, 31].

relevant x and Q^2 regions: 5% for the valence-quarks, 10% for the c and s quarks and 40% for the b quark, the corresponding uncertainties on the M_W measurement can be reduced to below 5 MeV, provided that a special observables and measurement procedures are employed. To reach this precision level, the required collected nucleon–nucleon luminosity should be larger than $100\,\mathrm{fb}^{-1}$.

Summarising, the use of the isoscalar nuclei beams could allow to achieve the accuracy in both the direct and indirect (through $\sin^2\theta^l_{\mathrm{eff}}$) W-boson mass measurements at the level better than 5 MeV, providing an important consistency test of the Standard Model as well as a stringent constraint for its possible BSM extensions.

3.7 New research opportunities with nuclear beams

The LHC research programme can be enriched by asking new questions and providing a suitable experimental framework to answer them. For example:

1. What is the mechanism which transmutes three degrees of freedom of the scalar field into the longitudinal-polarisation degrees of freedom of the W and Z bosons in the EW-vacuum ground state?

2. Is there any trace of such a mechanism which could be observed experimentally, e.g. by analysing the polarisation asymmetries in propagation of the transversely and longitudinally polarised EW bosons – both in the vacuum and in the matter?

To address such questions experimentally, the most desirable tool for generic exploration of the EW-boson sector would be a high-brightness polarisation-tagged beam of the EW bosons. If proton beams of energies exceeding 10^{17} GeV were available, such beams of the EW bosons could be easily formed and used in macroscopic experiments – in very close analogy to fixed-target muon-beam experiments which routinely use beams of unstable particles. Even if experiments using beams of the EW bosons cannot be realised at the macroscopic-length scales, the LHC offers a reduced-scope, yet unique, opportunity to realise them at the "femtoscopic"-length scales.

The LHC is a very efficient factory of the Z/W bosons, producing hundreds of millions of them over each year of its operation. Their polarisation can be controlled by measuring the recoil jet produced in their creation processes. The LHC unique merit is that these very short-lived particles can be observed – at the LHC beam energies – over a sufficiently long time to perform experimental "femtoscopic" studies of their properties and interactions.

The Z/W weak bosons travel – for the observers co-moving with the LHC bunches – over the atomic distances of up to 10^4 fm before decaying. This defines the maximal thickness, thus the type, of possible targets which, if arranged to co-move with the LHC bunches, could be employed in experimental studies of the properties and collisions of the EW bosons. Nature provides only one type of a target satisfying the above criteria – the bunches of partons confined in nuclear envelopes. Their flavour composition and the effective target thickness can be tuned using the nuclear partonic bunches of the variable nuclear atomic A and charge Z numbers, providing the analysing medium of the W and

Z boson properties. The formalism and the framework of such an analysis is discussed in details in [46].

It remains to be added that the use of the nuclei as the femtoscopic-length targets for experimental studies of the QCD colour-confinement mechanism was the principal initial goal of the development of the electron–ion collider (EIC) concept, first for HERA [17–21] and subsequently for RHIC [22–27, 29]. The most important condition to extend such studies to propagation of the EW bosons in the vacuum and the matter is to achieve a comparable partonic luminosity in collisions of the nuclear and proton beams.

3.8 LHC as photon–photon collider

The research domain where the superiority of the nuclear beams over the proton beams is the most evident is the photon–photon collision physics.

High-energy photon–photon collisions allow to test the Standard Model and to look for the presence of the BSM effects in a particularly clean way. In contrast to the quark and gluon collisions, photon–photon collisions are unaffected by the parasitic strong interaction effects. In addition, the matrix elements for photon–photon collisions can be predicted to the accuracy which is unreachable for processes involving quarks and gluons as initial partons. This allows to use the photon–photon collisions for the absolute measurement of the hadron-collider luminosity with the precision approaching the one achieved at the electron–positron colliders [47–49]. Moreover, the Z^2-enhancement of the photon content of the nuclear bunches, discussed in Section 2.3, is driven by peripheral processes in which the recoil nucleus does contribute to the energy deposition in the LHC detectors – the photon–photon collisions are thus not obscured by the collisions of spectator partons.

To illustrate the advantage of the nuclear bunches for studies of photon–photon collisions, in Fig. 4 we show the effective luminosity $4\pi^2 dL_{\gamma\gamma}/dW/W^2$ for the resonant photon–photon collisions at the LHC with the CM energy, W for the pp, CaCa and PbPb collisions [50].

The effective luminosity enhancement factors for the nuclear beams are very large – even if scaled down to the same nucleon–nucleon luminosity (the A^2 scaling), they are at the level of 200 for the PbPb collisions and of 60 for the CaCa collisions. They open several new research options at the LHC, including searches of axion-like dark-matter particles (ALPS), precision studies of the elastic light-by-light scattering and Higgs-boson production processes. The latter of these options is discussed in the next section.

3.9 Exclusive Higgs-boson production

Perhaps the most remarkable physics highlight of high-luminosity collisions of nuclear beams at the LHC would be to observe the exclusive production of the Higgs bosons in the photon–photon collisions and their background-free decays. Let us choose, for the discussion presented below, the case of the isoscalar calcium (Ca) beam.

In the high-luminosity proton–proton collision phase, the integrated luminosity of the order of $3000\,\mathrm{fb}^{-1}$ is expected to be delivered to the LHC experiments. If the same

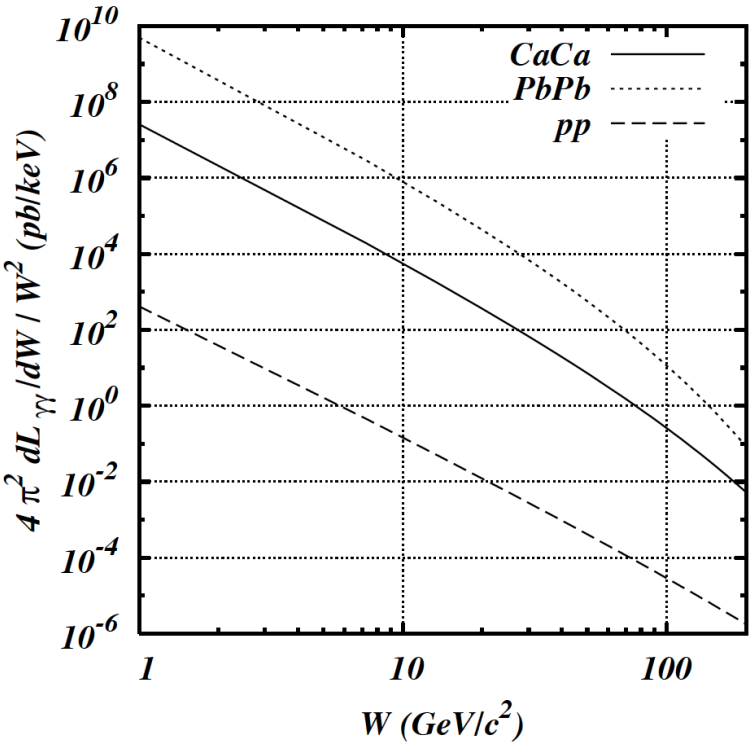

Figure 4: The effective luminosity for the resonance production in the photon–photon collisions as a function of the photon–photon collision centre-of-mass energy for the *pp*, CaCa and PbPb collision modes (for more details see [50]).

nucleon–nucleon luminosity can be achieved for collisions of the calcium beams and 30% of the running period is devoted to such a collision mode, the delivered CaCa luminosity would be $625\,\mathrm{pb}^{-1}$. The expected number of exclusively produced Higgs bosons, in such a scenario, would be $N_{\mathrm{Higgs}} \approx 420$ per experiment. In total 240, 90, 26 and 10 Higgs-boson decays to the $b\bar{b}$, WW^*, $\tau\tau$ and ZZ^* pairs, respectively, could be observed by each of the LHC experiments.

The above numbers are smaller, by large factors, than the corresponding numbers for the gluon–gluon collisions. However, the CaCa running mode could provide the first experimental evidence of the s-channel, exclusive, resonant Higgs-boson production in photon–photon collisions. Such an evidence would strengthen the interpretation of the 125 GeV-mass peaks observed in the gluon–gluon scattering channel as originating from the SM Higgs-boson decays. More importantly, the decays of the exclusively produced Higgs bosons can be easily identified and measured with negligible background[13]. This could facilitate the detection and the measurement of the $H \to b\bar{b}$ decay mode – the mode which is difficult to detect and measure in the gluonic collisions of the beam particles because of too a large irreducible background. According to our estimates, if only one twentieth of the pp running time in the high-luminosity mode would be attributed to the CaCa collisions, the $\gamma\gamma \to H \to b\bar{b}$ process could be discovered with more than the 5σ evidence. For more complete studies of the $\gamma\gamma \to H \to b\bar{b}$ discovery potential using nuclear beams at the LHC see e.g. [51].

Finally, let us add that the Higgs production cross-section and photon fluxes increase very fast with increasing energy of the ion beam. For the high-energy LHC, with the doubled beam energy, the expected number of produced Higgs particles increases by a factor of ≈ 10, opening the possibility of a competitive precision measurements of the Higgs-boson couplings.

3.10 QCD studies

The discussion of the relative merits of the proton and nuclear beams, presented so far, has been restricted to the SM EW and BSM sectors. For these sectors, the measurement of the beam particles' partonic distributions can be considered as the development of the specialised analysis tools, or even as an analysis burden, rather than a subject of dedicated studies. For the QCD sector, on the contrary, the measurement of partonic distributions is of pivotal importance.

Partonic distributions provide an unique insight into the mechanism of strong interactions of quarks and gluons which confines them in the nucleons and nuclei. They can be used for quantitative tests of the QCD predictions in the kinematical domains where the perturbative computational methods can be applied. More importantly, they are crucial for phenomenological studies of the strong interactions at large distance scales which can-

[13]It is important to note here that the expected number of CaCa collisions per bunch crossing is reduced with respect to the high-luminosity proton-beam collisions by a very large factor, allowing to observe exclusive photon–photon collision events without the need for very forward ion taggers. This aspect is discussed in more details in the subsequent section.

not be, at present, controlled by the available QCD computational methods. The merits of nuclear partonic bunches are of particular importance for these studies.

The data collected so far at the LHC in the low-luminosity pPb and PbPb collision runs for the Drell–Yan production of on-shell and off-shell EW bosons – which could potentially probe partonic distributions with high precision – are suffering from large statistical errors. The LHC nuclear collision data have, so far, hardly added any new knowledge to that acquired from the analysis of the fixed-target data collected in the pre-LHC era [52].

The high-luminosity collisions of nuclear bunches would open new perspectives for the QCD studies at the LHC. Their highlights include:

- The validity test of the QCD DGLAP equations [15] describing the Q^2-evolution of partonic distributions could be extended to the "high partonic density regime" involving partons carrying a small fraction of the nucleus momentum.

- Studies of the colour conductivity effects [53] in nuclei, by comparing the measured partonic distributions in their central and peripheral collisions.

- Precise measurement of the QCD coupling constant α_s, by measuring the inclusive spectra of leptons produced in collisions of isoscalar nuclei [33].

- Studies of the relative density of protons and neutrons in the centre and on the surface of the nucleus, and the corresponding studies of the neutron skin effect [54], by measuring the asymmetries in the transverse momentum distributions of positively and negatively charged W-bosons in collisions of isoscalar beams.

- Studies of the mechanism of binding nucleons within nuclei, by precision measurement of the $R^A_{v,s}$ factors (see Eq. (2.4)) in the wide domain of x and Q^2 variables, with the significantly higher precision than that achieved so far.

Last but not least, the high-luminosity collisions of light nuclei could provide a new environment to study the quark–gluon plasma signatures, by enabling the observation of rare collision events with abnormally high particle multiplicities. Such studies would complement the studies of the quark–gluon plasma signatures in the low-luminosity collisions of heavy nuclei.

3.11 Pile-up background

The precision of the EW measurements and the sensitivity of searches for the BSM processes in the high-luminosity pp-collision phase of the LHC operation will suffer from the large pile-up background. Already in the present phase of the LHC operation with proton beams, a collision event of interest is accompanied on average by $\nu = 30$ background pile-up collision events occurring within the time of the bunch crossing of $\approx 700\,\text{ps}$. They give rise to energy depositions in the LHC detectors which, in a majority of cases, cannot be unambiguously attributed to the signal and background events. In addition, they

produce a large number of hits in the LHC detectors trackers – a severe problem for fast track-finding algorithms affecting the trigger and event selection efficiency. In the high-luminosity LHC phase, with the 50 ns interval between the beam bunches, ν is expected to rise to the value of 454 [55]. Since the LHC detectors cannot cope with such a pile-up rate, the LHC luminosity will have to be levelled to value of $2.5 \times 10^{34}\,\mathrm{cm}^{-2}\mathrm{s}^{-1}$. For this luminosity, the pile-up will be reduced to $\nu = 150$ – the value that is sustainable for the LHC-detectors operation. For the alternative high-luminosity LHC operation with the 25 ns bunch-spacing, the levelled luminosity is expected to be twice larger (at the same ν value).

A very important merit of nuclear beams is that the number of collisions per bunch crossing can be drastically reduced while preserving the same nucleon–nucleon luminosity in the AA collision mode as in the pp one. The relationship between ν_{AA} and ν_{pp} can expressed, for the same nucleon–nucleon luminosity, as follows:

$$\nu_{AA} = \nu_{pp} \times \frac{\sigma_{AA}}{\sigma_{pp}} \times A^{-2}, \tag{3.7}$$

where σ_{AA} and σ_{pp} are the respective inelastic cross sections of the AA and pp collisions, respectively. The number of collisions per bunch-crossing decreases with the increasing atomic number proportionally to $A^{-4/3}$ – by a factor of 40, 136, 650 and 1260 for the OO, CaCa, XeXe and PbPb collisions, respectively. Such a large reduction factors open the possibility of observing exclusive peripheral collisions of nuclei at the high nucleon–nucleon luminosity in a pile-up free mode.

The decrease of the ν value is, of course, associated with an increase of multiplicity of particles produced in each of the AA collisions. However, at the *high nucleon–nucleon luminosity*, the average total multiplicity of background particles per bunch-crossing produced in the fiducial volume of the LHC trackers turns out to be smaller for the AA collisions than for the pp collisions (for the same effective nucleon–nucleon luminosity).

The above statement is, at first sight, counter-intuitive and requires further explanation. For the low nucleon–nucleon luminosity, defined by the condition $\nu_{pp} \leq 1$, the opposite is true because the number of background particles produced in a single AA collision is significantly higher that that in a single pp collision.

At high luminosity, when ν_{pp} is larger than the atomic mass number A of the colliding nuclei, it matter less whether colliding partons are delivered to the interaction point in the proton or in the nuclear envelopes. The multiplicity of background particles per bunch-crossing is expected to be driven by the number binary collisions, N_{coll}, of free (the proton case) and bound (the nuclear case) nucleons. The bound nucleons undergo soft collisions several times over their passage through the volume of the target nucleus. They "loose" their soft partons already in their first collision and produce less particles per binary collisions than free nucleons (protons)[14]. For nuclear bunches, the number of produced particles is no longer proportional to the number of binary collisions but, instead, to the number of pairs of wounded (participant) nucleons [57], $N_{\mathrm{part}}/2$. The

[14]One of us (MWK) is indebted to Wit Busza for a discussion of the multiplicity of particles produced in pp and AA collisions.

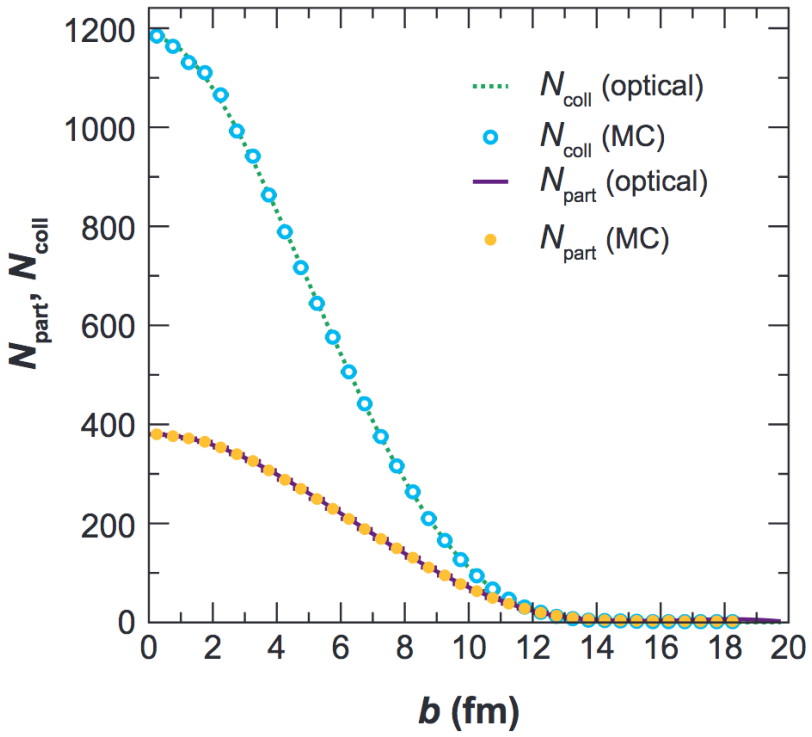

Figure 5: The number of binary collisions $N_{\rm coll}$ and the number of collisions participants $N_{\rm part}$ as a function of the impact parameter, calculated in the optical approximation (lines) and with a Glauber Monte Carlo (symbols) for the AuAu collisions, taken from [56].) Note that $N_{\rm coll}$ is a measure of the nucleon–nucleon luminosity, both for the pp and AA collisions. The ratio $N_{\rm part}/N_{\rm coll}$ is thus the expected reduction factor of particle multiplicity in the central region in the AA collisions with respect to the pp collisions.

difference of $N_{\rm coll}$ and $N_{\rm part}$ for the AuAu collisions is shown if Fig. 5. $N_{\rm part}/2$, driving the background level for AA collisions, is significantly smaller than $N_{\rm coll}$, determining – for the equivalent nucleon–nucleon luminosity – the background level in the pp collisions. The background reduction is expected to be particularly significant in the central AA collisions characterised by a small impact parameter b of the colliding nuclei. On average, we expect the reduction of the pile-up background level for the gold (Au) beams by a factor of 4 as compared to the one for the 50 ns bunch-spacing pp operation mode and by a factor of 2 as compared to the 25 ns one. This would allow to operate the LHC detectors at higher nucleon–nucleon luminosity by using the nuclear rather than proton partonic bunches.

4 Towards high-luminosity AA collision scheme

4.1 Introductory remarks

In order to consider seriously a scenario of sharing the LHC running time between the pp and AA collision modes in the high-luminosity phase of its operation, and to fully profit from the numerous merits of nuclear beams, put in light in the previous section, a new AA beam-collision scheme has to be proposed which satisfies the achievable luminosity requirement specified by the following condition:

$$L_{AA} = L_{NN}/A^2 \approx L_{pp}/A^2, \tag{4.1}$$

where: L_{AA}, L_{NN} and L_{pp} are, respectively, the nucleus–nucleus, effective nucleon–nucleon and pp luminosity in the high-luminosity phase of the LHC operation. This condition assures a comparable partonic luminosities for the pp and AA collisions and, as a consequence, both the equivalent statistical precision of the EW measurements and the equivalent sensitivity to the BSM effects[15].

The concept of such a scheme will be presented in this section. Prior to its discussion a more general comment is, however, mandatory.

The pp collision mode is the only one to search for the BSM effects at the highest partonic-collision CM energy $\sqrt{s} \geq 3$ TeV, not accessible for the AA collision mode. It is also clearly superior for the precision measurements of the EW processes for which the cross section is a strongly rising function of $\sqrt{s}$, such as e.g. the production of triplets of the EW bosons. Therefore, it will always remain the principal running mode of the LHC. However, if the AA collision luminosity target, specified above, can be achieved, then devoting of the order of 30% of the pp running time to the AA mode would have a negligible impact of the pp collision results, while opening new research domains specific to the AA collision mode.

[15]As discussed in Section 3.1, the equivalence of the pp and AA collision modes is restricted to the kinematical domains which are accessible to both collision modes and where the partonic-luminosity penalty factors are close to 1.

The above argument is strengthen by the lack of evidence of any BSM anomaly in the *pp*-mode exclusivity domain in the data collected so far at the LHC. That is why, in our view, complementary LHC running modes should be studied and – if their viability is experimentally proven – incorporated in the LHC operation planning.

4.2 Optimisation parameters

The nucleon–nucleon luminosity in the *pp* and *AA* collisions of bunched beams can be specified by the following expression:

$$L_{NN} = f_0 \gamma_L n_b \frac{N_N^2}{4\pi\epsilon_n \beta^*} H\left(\frac{\sigma_z}{\beta^*}, \theta_c\right), \tag{4.2}$$

where f_0 is the beam revolution frequency, γ_L is the beam Lorentz factor, n_b is the number of colliding bunches, N_N is the number of nucleons in the bunch ($N_N = N_p$ for the proton bunches and $N_N = AN_A$ for the nuclear bunches), ϵ_n is the normalised transverse emittance of the beams, β^* is the value of the beta function at an interaction point and the function $H(\sigma_z/\beta^*, \theta_c)$ describes the geometrical luminosity reduction – driven by a non-zero beam crossing angle θ_c and by the hourglass effect. For the definitions of the accelerator physics terms and parameters used in this paper see the very recent review "Modern and Future Colliders" by Vladimir Shiltsev and Frank Zimmermann [58] and references quoted therein.

In the following we shall assume the same interaction-point (IP) optics, the small beam crossing angle and the same number of bunches for the proton and nuclear beams[16]. Under these assumptions the ratio of the NN and *pp* luminosities can be expressed as

$$\frac{L_{NN}}{L_{pp}} = \frac{\gamma_L^A}{\gamma_L^p} \times \frac{A^2 N_A^2}{N_p^2} \times \frac{\epsilon_n^p}{\epsilon_n^A}. \tag{4.3}$$

For the HL-LHC *pp* operation mode one expects: $N_p = 3.5 \times 10^{11}$ (50 ns bunch bunch separation) and $\epsilon_n^p = 3\,\text{mm mrad}$ [55]. The expected *pp* operation peak luminosity (without a crab-cavity) is $L_{pp} = 8.4 \times 10^{34}\,\text{cm}^{-2}\text{s}^{-1}$. Achieving a comparable NN luminosity in AA collisions without modifying the beam collision optics is anything but easy. It will require increasing of the nuclear-bunch population N_A or reduction of the nuclear-beam transverse emittance, ϵ_n^{ion}, or both. The present and the target values for the number of nuclei per bunch and the transverse emittance of the nuclear beams at the LHC are discussed in the following section.

4.3 Bunch intensity

The quest for the maximum intensity of the nuclear (ion) beams is limited by many inter-correlated effects which affect both the single-beam-particle and bunch dynamics.

[16]The high-luminosity LHC *pp* operation mode with 50 ns bunch spacing foresees 1404 bunches [55] while the AA mode 1232 bunches [64].

The bunch-intensity limit in the LHC injectors depends strongly on: (1) the technical, Z-dependent constraints of the present LHC injectors; (2) the stripping stages of the ion beam which must be optimised to circumvent the bunch space-charge constraints; (3) intra-beam scattering constraints; (4) beam losses due to electron stripping in the collisions of the beam particles with the residual gas in the LHC injector rings and (5) several other less important effects. The precise assessment of the achievable N_A values can be done on ion-by-ion bases by empirical optimisation of the operation mode of the ion source and the full LHC injection chain.

The deuteron beam, an obvious candidate for the research programme advocated in Section 3, cannot meet the luminosity requirement expressed in Eq. (4.1) for the reasons explained below.

The dedicated studies presented in Ref. [59] showed that Linac4 [60], providing highly efficient acceleration of the H^- ion beam[17], is not a feasible candidate for accelerating D^- ion beam. The reason is that, while providing good longitudinal acceptance for ions injected at a half of the proton injection velocity, the transverse RF-defocusing of the beam would be too strong, resulting in the excessive transverse beam losses. This leaves Linac3 [61], optimised for heavy ions, as the only option to accelerate the deuteron beam. The initial estimate presented in Ref. [62] shows that the achievable N_A value for deuteron bunches would be in the range $0.3 \times 10^{10} \leq N_D \leq 1.5 \times 10^{10}$. The expected number of nucleons per deuteron bunch would thus be by a factor of 12–60 lower than that for the proton beam. If the beam emittance stays the same for both beams, the L_{NN} value for duteron–deuteron collisions at the LHC would be by a factor of 288–7200 lower than the L_{pp} value. Such a luminosity drop cannot, obviously, be compensated by the corresponding reduction of the beam transverse emittance. The deuteron-beam colision option is thus discarded from the further discussion presented in this paper. A similar conclusion is valid also for the helium beam, for which a poor transmission in Linac3 was reported in Ref. [63].

The present knowledge accumulated at CERN while running $Z \geq 8$ ion beams can be expressed by the empirical formula [64] relating the ion-bunch intensity for an arbitrary nucleus to the achieved value for the Pb($A = 208, Z = 82$) bunches, $N_{\rm Pb} = 1.9 \times 10^8$:

$$N_A(Z, A) = N_{\rm Pb} \times \left(\frac{Z}{82}\right)^{-1.9} . \tag{4.4}$$

The expected numbers of nucleons per bunch according to the above formula are smaller than that for the proton beam: by a factor 1.4 for the oxygen, 3.2 for the calcium, 6.5 for the krypton and 8.8 for the xenon bunches. Thus, to achieve the comparable NN luminosity in the AA collision mode as that in the pp mode with the present CERN ion-beam source and the LEIR ring, the only way forward is to try to compensate the bunch population decrease (w.r.t. the proton bunches) by the corresponding decrease of the transverse beam emittance. While for the highest-Z beams this is very hard, if not

[17]Protons for the high-luminosity LHC operations are initially accelerated as H^- ions, carrying two attached electrons. Following the Linac4 acceleration phase the electrons are stripped off.

imposible, to achieve, for the low-Z ones, such as the beams of oxygen and calcium, it is worth trying.

4.4 Beam emittance

Two questions have to be addressed while considering the high-luminosity option of the LHC with the low-emittance nuclear beams. The first is how to reduce the transverse beam emittance of colliding beams. This will be discussed in the next section. The second, discussed below, is how to preserve the beam emittance in the presence of the intra-beam scattering.

Let us assume, for a while, the same IP lattice parameters, the same number of nucleons and the same bunch emittances for the proton and ion beams colliding at their maximal energies related to each other by $\gamma_L^A = (Z/A)\gamma_L^p$. The relationship of the emittance-growth parameter, defined as $\alpha_{\rm IBS} = 1/\epsilon \times d\epsilon/dt$, for the ion and proton beams is well approximated by[18]

$$\alpha_{\rm IBS}^A = \frac{Z^3}{A^2} \times \alpha_{\rm IBS}^p. \tag{4.5}$$

The emittance growth is stronger for the ion beam than for the proton beam for the same number of nucleons in their respective bunches: by a factor of 2 for the oxygen, 5 for the calcium, 9.5 for the xenon and 12.7 for the lead bunches. However, for the realistic $N_A(Z, A)$, discussed in the previous section, the emittance growth for the proton and for the ion beams become comparable – they are larger for the latter by a factor of: 1.4 for the oxygen, 1.6 for the calcium, 1.5 for the xenon and 1.4 for the lead bunches.

For the normalised emittance of the proton beam in the high-luminosity phase of the LHC operation of 3 mm mrad, the expected emittance growth rate is 17.2 hours [55]. There is thus a room to compensate reduction of the number of nucleons in the ion-beam bunches by colliding the ions beams with the reduced transverse beam emittance, w.r.t. to that for the proton beam, within tolerable emittance growth boundaries. This is the path that will be explored in the following.

4.5 The proposed scheme

The emittance of the bunched beams is determined by the beam-source emittance and by its growth over the bunched-beam acceleration and the storage time. To reduce their transverse emittance, the beams have to be cooled. There are several methods to cool ion beams. In the initial stage of ion beam acceleration (LEIR ring) the electron cooling method is used. The corresponding reduction of the beam emittance is, however, insufficient and done "too early" in the beam acceleration cycle to be preserved over the subsequent phases of the beam acceleration in the PS and SPS rings. The LEIR cooling

[18] One of us (MWK) is indebted to John Jowett for illuminating discussions on the emittance growth rate in the CERN accelerator rings.

must thus be complemented by another cooling method, optimally in the advanced stage of the beam acceleration process[19].

In this paper we propose to reduce the beam transverse emittance by laser cooling, exploiting *the atomic degrees of freedom* of the beam particles[20].

The final stripping of the electrons attached to their parent nuclei, being routinely done in the PS–SPS beam-transfer line is, in the proposed scheme, postponed and follows the beam cooling phase. Ideally, the optimal phase for the beam cooling would be when the beam is accelerated to its top LHC energy. Unfortunately, the subserquent collisions of the atomic beams in the LHC interaction points would lead to too a high rate of the electron stripping in beam–beam collisions – the lifetime of such beams would be lower than a couple of seconds [65]. Therefore, we propose to cool the atomic beam at the top SPS energy and, subsequently, to strip the remaining electron(s) in the transfer line between the SPS and the LHC. The fully stripped ion beam is then accelerated to its maximal energy at the LHC. In such a scheme, a care should be taken to reduce, as much as possible, the emittance growth in the LHC bunch collection and acceleration phase (e.g. by the controlled longitudinal emittance blow up during the bunch collection and ramping time), and, if necessary, to reduce the emittance growth over the beam collision run by the conventional stochastic cooling method [66–68], or by the optical stochastic cooling method [69].

5 Laser cooling of ultra-relativistic atomic beams

Laser cooling is a well-known technique in the atomic physics. It has been successfully used to cool beams of weakly relativistic ions [9, 10] and there are plans to use this technique by the GSI FAIR project [70] for moderately relativistic ones. At the SPS, where the maximum Lorentz factor of the ion beam reaches the value of $\gamma_L \approx 200$, the ions are highly relativistic. Cooling of highly relativistic ion beams has not been experimentally studied so far.

The laser cooling is based on resonant absorption of the laser photons by the beam particles and by subsequent emission of photos. The cross section for this process is very large if the energy of the photons is tuned to the resonant atomic transitions of the beam particles. Therefore, to achieve the fast and efficient cooling, the ions have to carry, during the beam-cooling phase, a fraction of their attached electrons. Such ions are, in the following, called partially stripped ions (PSIs). The kinematics and dynamics of the photon absorption and emission process is presented in Appendix B.

The PSI energy loss due to emission of the photon is very small as compared to its energy. However, over multiple turns in the storage rings, even a small energy loos can significantly influence the PSI-beam dynamics. The laser cooling mechanism is similar

[19] With the increase of the beam energy, the rate of the intra-beam scattering (IBS) decreases proportionally to the Lorentz γ_L-factor, reducing significantly the "post-cooling-phase" emittance growth.

[20] Such a cooling method can be applied only for the ion beams – the proton beams are excluded because H^- ions cannot be accelerated in the CERN circular machines.

to that of the synchrotron-radiation cooling for the electron beam. The most notable difference is that while the latter is a spontaneous (random) process, the former can be stimulated and precisely controlled by the suitable tuning of the laser pulse parameters, such as its power, the photon-wavelength spread and offset, the photon transverse spot size and its offset with respect to the ion-beam spot. This allows to selectively manipulate a chosen fraction of ions within their bunches with an unprecedented precision.

5.1 Longitudinal cooling

Energy loss of the PSI, absorbing and re-emitting the photon, grows as γ_L^2. Since the higher-energy ions loose energy faster than the lower-energy ones, this naturally leads to the reduction of the energy spread of the PSI beam [71].

In the bunched beam, the PSI energy experiences synchrotron oscillations (around the central energy) which are coupled with the longitudinal oscillations. Therefore, the reduction of the energy spread also leads to the reduction of the longitudinal bunch size. The rate of such cooling is slow – the typical cooling time is equal to the time it takes to radiate the full ion energy.

A leap in the cooling speed can be achieved by exciting intentionally only the fraction of the ions – those which carry the energy larger than the central value of their energy spread. This is possible because the width of the atomic transition and the laser-photon energy band can be tuned to be much narrower than the energy spread in the ion beam. In this case, the cooling time is comparable to the time which is necessary to radiate a fraction of the ion energy, which is of the order of the relative energy spread of the ion beam: $\sim 10^{-4}$–10^{-5}. The improvement of the cooling speed is illustrated in Fig. 6.

5.2 Transverse cooling

The transverse beam cooling accompany, in a natural way, the longitudinal one because the effective friction force due the emission of photons is directed opposite to the ion momentum vector, while the RF-cavity restores only its longitudinal component. This type of cooling is, however, too slow to be used at the SPS flat-top energy[21].

The cooling scheme which allows to shorten the cooling time below 15 seconds is based on the dispersive coupling of transverse and longitudinal oscillations in a storage ring [73]. The mechanism of the longitudinal–horizontal coupling through dispersion is illustrated in Fig. 7. The horizontal betatron oscillations are first converted into energy (synchrotron) oscillations and then the synchrotron oscillations are suppressed quickly using the fast longitudinal cooling method described in the previous subsection. This scheme requires

[21]The resistive power dissipated in the main SPS dipoles and the quadrupoles at the top SPS energy is 44 MW. The SPS beam can be coasted at this energy (using the pulsed magnet operation mode) over the time interval which should be shorter than $\tau_{coast} \approx 15$ seconds. As a consequence, the beam cooling phase must be finalised within this time interval. A fallback solution would be to cool the beam at the energy below the value $E_{\rm beam} = 270 \times Z\,{\rm GeV}$, at which the beam can be permanently coasted, and resume the acceleration up to the LHC injection energy following the beam-cooling phase.

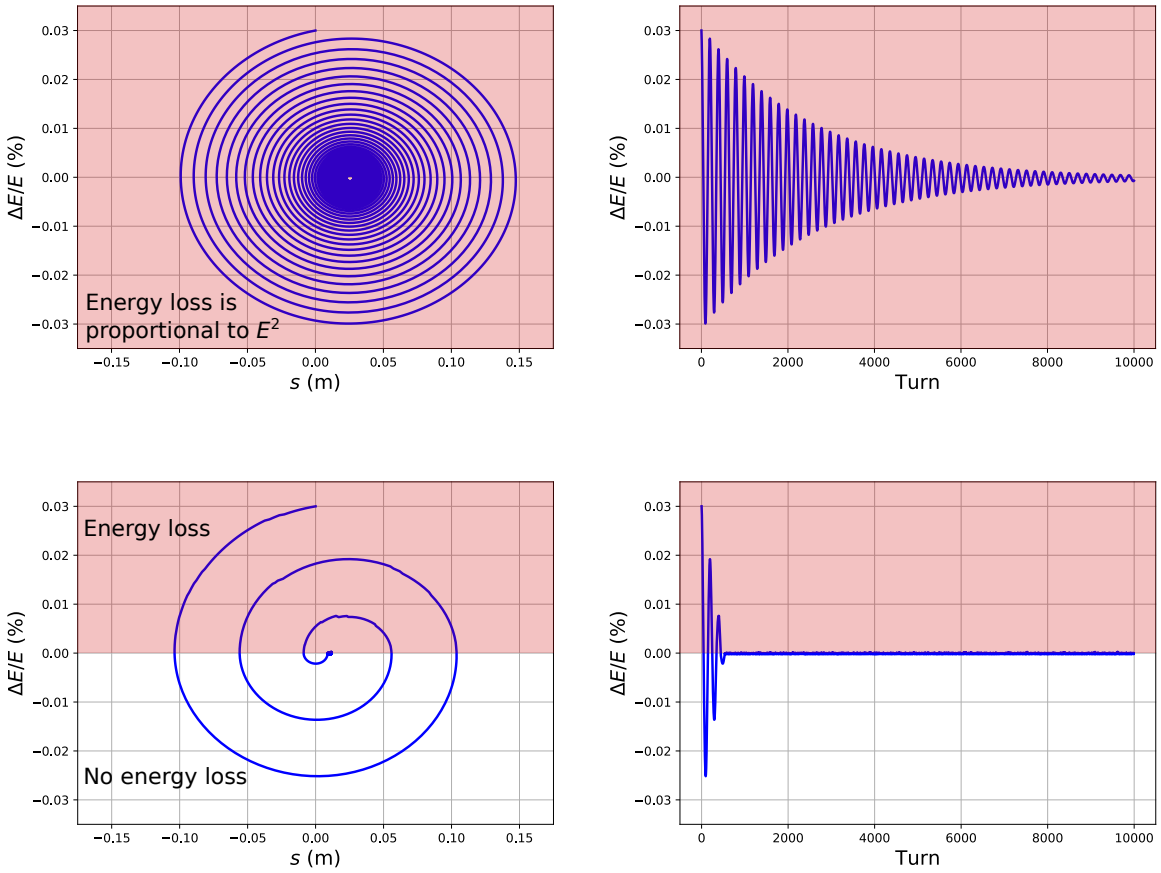

Figure 6: The evolution of the energy and the longitudinal position of the ion, relative to their central values, as a function of the turn number in the storage ring, for two regimes of the laser cooling. The top plots show the broad-band laser cooling [71] using the laser frequency band which is large enough to excite all the ions, disrespectful of their energies. The bottom plots show the regime of fast cooling [72] using the laser frequency band which has a sharp cut-off, positioned such that the ion absorbs the laser photon only if the ion energy is above its central value.

two different lasers and two different photon–PSI interaction points. The focal point of the first-laser beam is shifted towards the negative horizontal position with respect to the ion beam centre (for a positive value of the dispersion function) by a value of Δx. This laser has a broad frequency spectrum allowing to excite the ions over the full spread of their energies. The focal point of of the second-laser beam is centred on the ion beam axis. Its frequency band is tuned to excite only those of the ions which carry the energy above its central value.

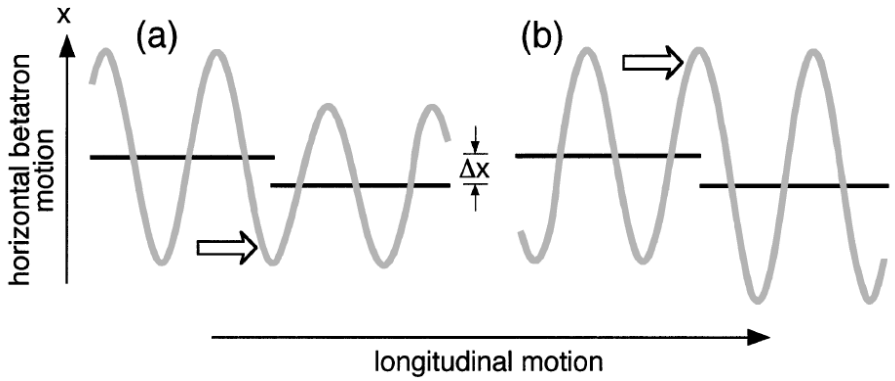

Figure 7: Horizontal betatron oscillations of a stored ion around the central orbit in a region with positive dispersion. The moment of photon emission and the corresponding change of the central orbit is indicated by the arrow. A reduction of the amplitude of the oscillation occurs when an ion radiates a photon at a negative ($x < 0$) phase of the betatron oscillation (a). If the photon is emitted at $x > 0$ (b), then the amplitude of the betatron oscillations is increased. The transverse cooling will occur if more photons are emitted at $x < 0$ than at $x > 0$. (Adapted from [73].)

In order to suppress the vertical betatron oscillations, one needs to couple them to the horizontal ones using the transverse betatron coupling resonance. To achieve an efficient coupling, the frequency of the vertical betatron oscillations should be close enough to the frequency of the horizontal betatron oscillations.

5.3 Beam cooling R&D in Gamma Factory PoP experiment

Evaluation of various techniques of the longitudinal and transverse cooling of atomic beams at ultra-relativistic energies will soon be addressed in the forthcoming R&D phase of the Gamma Factory project [1, 12] – in its Proof-of-Principle (PoP) experiment [13].

This experiment plans to use the lithium-like lead beam, Pb^{79+}. The lithium-like lead beam has been chosen because it can be produced and accelerated at CERN with a minor change of the present operation mode of the fully stripped lead beams. The results of this experiment will then be extrapolated to other ion species specified by A, Z and the number of left electrons N_e. The extrapolation results will determine, together with other beam operation aspects discussed in the next section, the most optimal ion-beam candidate for the high-luminosity LHC collisions of nuclear beams.

6 Operation constraints

6.1 Parasitic beam burning

The increase of the luminosity in collisions of nuclear partonic bunches would be useless if a dominant fraction of the beam particles were "burned-off" in those of the ultra-peripheral collisions which change the magnetic rigidity of the beam particles. Such processes give rise to beam losses in the cold sections of LHC rings and represent a serious danger for the operation of the LHC superconducting magnets. These processes have been extensively discussed in [74].

The electron–positron pair production in which the electron is bound to one of the colliding nuclei has already been a principal luminosity limiting factor – already for the low-luminosity PbPb collisions at the LHC. The cross section of this process decreases very quickly with the decreasing charge of the nucleus, proportionally to Z^7. While prohibiting the use of the Pb beam for the high-luminosity mode of the LHC, it becomes negligible for low-Z ions.

For low-Z ions, the process of photon-induced dissociation of the nucleus with emission of a single neutron or a pair of neutrons – having a less strong Z^3-dependence – is the dominant parasitic beam burning process. The neutron-loss cross section is larger than the inelastic cross section for ions heavier than krypton – for lighter ions it is less important, e.g. it represents only 38% of the total cross section for the CaCa collisions and 5% for the OO collisions.

We thus conclude that the parasitic beam burning processes does not represent an obstacle for the high-luminosity collisions of partonic nuclear bunches provided that ions with $Z \leq 25$ are used in such a scheme.

6.2 Photon fluxes revisited

As discussed in Section 3.8, in order to maximise the photon–photon luminosity, which is proportional to Z^4, large-Z ions appear to be the best beam candidates. However, given the beam-burning constraint discussed above, the optimal Z of the ion beam should represent a compromise between the photon–photon luminosity increase due to the charge-coherence effects and the "allowed" luminosity limits driven by the parasitic beam-burning processes. Such a compromise was discussed already long time ago in [75] for the case of two beam-burning collision points[22].

The highest effective photon–photon luminosity, for the beam operation model presented in [75], can be achieved for the CaCa collisions, see Fig. 8. It was found to be larger by a factor of ≈ 10 w.r.t. the PbPb collisions and by a factor of ≈ 30 w.r.t. the pp collisions. In reality, if no new forward ion detectors are designed and constructed for the high-luminosity phase of the LHC operation, the increase of the effective photon–photon

[22]One of the authors (MWK) acknowledges numerous discussions with Daniel Brandt on the use of light nuclei for the DESY, BNL and CERN research programmes at the time of designing the running modes for the EIC project for DESY and later for BNL.

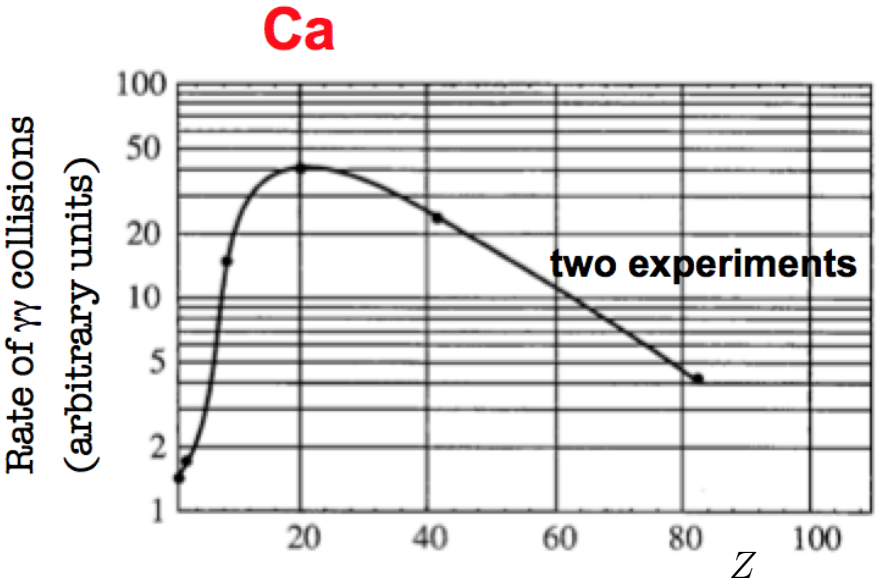

Figure 8: The Z-dependence of the effective rate of the photon–photon collisions for the operation scenario discussed in [75].

luminosity in the "coherent-photon" kinematical domain is by far more significant. For the collisions of the calcium ions, the "useful" photon–photon luminosity is expected to be by a factor of ≈ 4000 larger than that for the the pp collisions at the equivalent nucleon–nucleon luminosity[23].

6.3 Laser constraints

The beam-cooling process discussed in Section 5 is based on resonant excitations of the PSIs stored in the SPS ring by laser photons. The maximal energy, $E^p_{\rm max}$, of the SPS proton beam and the wavelengths range of commercially available visible and near-infrared high-power lasers, $440\,{\rm nm} \le \lambda \le 3000\,{\rm nm}$, constrain the minimal number of electrons which have to remain attached to their parent ions, N_e, at the SPS phase of the beam acceleration via the following condition:

$$440 < \frac{hcE^p_{\rm max}}{M_{\rm ion}Ry} \times \frac{Z-N_e}{AZ^2} \times (1+\cos\theta) \times \frac{n_1^2(N_e)\,n_2^2}{n_2^2 - n_1^2(N_e)} < 3000, \qquad (6.1)$$

where $M_{\rm ion}$ is the ion mass, Ry is the Rydberg constant, θ is the collision angle of the laser-photon beam and the PSI beam, $n_1(N_e)$ is the Bohr radial number of the ground state of the last (most loosely bound) of the N_e electrons occupying the Pauli allowed levels and n_2 is the Bohr radial number of excited state.

[23]Photon–photon collisions can be efficiently selected and measured only in the case of one beam particle collision per bunch crossing – we remind that for the nucleon–nucleon luminosity of $2.5 \times 10^{34}\,{\rm cm}^{-2}{\rm s}^{-1}$, the event pile-up rate amounts to $\nu = 150$ for the pp collisions and $\nu = 3.3$ for the CaCa collisions.

The laser technology constraints do not restrict the Z and A range of ions which can be cooled at the SPS. It restricts, however, the number of electrons attached to their parent nuclei in the cooling phase of the beam. The number of electrons, N_e, must rise with the increasing Z of the beam particles, such that the increase of $n_1(N_e)$ compensates the Z^2-rise of the electron binding energies. In practice, the beam of the hydrogen-like, $N_e = 1$, and the helium-like, $N_e = 2$, oxygen ions can be cooled at the SPS with nearly head-on photon–ion collision angle. The minimal N_e rises to 3 for the calcium ions and to 11 (fully filled the $n = 1$ and $n = 2$ atomic levels) for the krypton ions[24].

6.4 Beam lifetime

For the SPS ring, where the pressure of the residual gas molecules stays at the level of 10^{-8} mbar (three order of magnitude higher than in the LEIR and the LHC), there is a price to pay for the increase of the number of electrons attached to their parent nucleus – necessary for high-Z ions – the beam-lifetime decrease below the SPS acceleration cycle length.

The Gamma Factory group has performed dedicated machine studies with partially stripped ion beams allowing to validate and calibrate the software tools used in calculation of the beam lifetime for arbitrary Z, A and the number of left electrons, N_e [76].

In 2017 the $^{129}Xe^{39+}$ atomic beam was accelerated, stored in the SPS and studied at different flat-top energies [77–79]. The analysis of the measured lifetime constrained the molecular composition of the residual gas in the SPS rings. In 2018, the $^{208}Pb^{81+}$ and $^{208}Pb^{80+}$ beams were successfully injected to the SPS and accelerated to 270 GeV proton-equivalent energy. The observed lifetimes of the $^{208}Pb^{80+}$ and $^{208}Pb^{81+}$ beams of, respectively, 350 ± 50 and 600 ± 30 seconds agreed with the predictions based on the calibrated molecular composition of the SPS vacuum [80].

The observed agreement allowed us to extrapolate the results of the SPS beam tests to arbitrary Z and N_e. For high-Z ions, such as xenon or lead, and high N_e, required to satisfy the laser technology constrains discussed in Section 6.3, the beam lifetime decreases significantly below the SPS cycle length for the LHC injection which is, at present, approximately 20 seconds. For the very low-Z ions, lighter than oxygen, the electrons become too loosely attached to their nuclei and no matter how many electrons are left attached, the SPS beam lifetime will always be shorter than the SPS cycle length[25].

The "sweet spot" where the beam lifetime and the laser technology constraints are both satisfied is restricted to a very narrow region around $Z = 20$. For the present SPS vacuum conditions, the predicted lifetime of $^{40}Ca^{17+}$ beam is 16 ± 10 seconds. If the SPS cycle length for the LHC injection is unchanged, the SPS vacuum quality would have to

[24]These restrictions are important only for radial atomic excitations. For the excitation which do not change the Bohr radial number and which are driven by spin-orbit interactions, the $N_e = 3$ limit can be kept even for the highest Z ions, at the expense of significantly higher laser power requirement. This option will be used in the Gamma Factory PoP experiment, and is not discussed in the present paper.

[25]We are indebted to Slava Shevelko for his guidance and his calculations of the lifetimes of the partially stripped ions in the SPS.

be improved by at least a factor of two to reduce the beam losses over the SPS stacking, acceleration and the cooling phases[26].

7 High-luminosity CaCa collision scheme

The calcium (isoscalar nuclear) beam satisfy the operation constraints, discussed in the previous section and, in addition, has numerous merits for the physics programme at the LHC, discussed in details in Section 3. It is by far the most optimal candidate for the high-luminosity operation of the LHC with a nuclear beam.

In this section we present a concrete scenario of producing, accelerating, cooling and colliding the calcium beams at the LHC. The Ca beams have never been produced at CERN. A more detailed scenario of their operation in the CERN accelerator complex can only be worked out by the CERN accelerator experts. In this section we identify the most critical points which would need to be addressed by such studies and which are critical to prepare the calcium beam for the cooling phase in the SPS, and for its subsequent injection to the LHC. We discuss also a concrete laser beam-cooling scheme of the $^{40}Ca^{17+}$ beam and evaluate its expected performance.

7.1 Calcium source

The present CERN Linac 3 ion source is an 14.5 GHz ECR source optimised to produce the lead beams. The ECR source uses a long microwave heating pulse of 50 ms which ionises lead atoms to the highest achievable charge states and subsequently forms 1 ms long ion-beam pulses. To match the pulse length to the Low Energy Ion Ring (LEIR) requirements only 1/5 of this pulse is accelerated in Linac 3 and injected to LEIR. This scheme can be used for the operation of the calcium source.

The required isoscalar calcium isotope of $^{40}_{20}$Ca has an abundance of 96.9%. The vapour pressure for calcium is higher than for lead, such that the ovens could be run ~ 80 K cooler for the same vapour pressure [81]. The change of the lead rod to the calcium rod is, in principle, easy but a setting-up time would be necessary for the overall optimisation of the source yield.

The relative yields of principal-charge states after stripping of electrons at the exit of Linac 3 can be predicted by assuming the input energy of 4.2 MeV/u and the equilibrium charge state after stripping:

Model	Ca^{16+}	Ca^{17+}	Ca^{18+}
Baron *et al.* [82]	13%	38%	36%
Schiwietz *et al.* [83]	20%	34%	27%

It is important to note that the requisite charge state for the laser cooling at the SPS, Ca^{17+}, can already be achieved at the exit of Linac 3 with the maximal efficiency.

[26] The concentration of the vacuum molecules over the historical runs of the SPS at the $p\bar{p}$ collider was lower by a factor of about 10 with respect to the present values.

Therefore, contrary to the lead beam, no additional electron stripping is required in the PS-to-SPS transfer line.

7.2 Ca^{17+} beam in LEIR, PS and SPS

LEIR receives long pulses of ions from Linac 3 and transforms its long pulses into high-brilliance bunches by means of multi-turn injection, electron cooling and accumulation. Important issues which would need to be addressed for the LEIR and PS acceleration phase of the Ca^{17+} beam, with respect to the canonical operation of the Pb^{54+} beam, are the space-charge effects and the beam transfer limitations.

The *space-charge tune shift parameter*, $\Delta Q_{\rm SC}$, rises proportionally – at the fixed bunch longitudinal and transverse emittance – to Z^2 and $N_{ion}(Z, A)$, and inversely proportionally to A and γ_L^3. The tune shift parameter for the Ca^{17+} bunches of the same ion population as the Pb^{54+} bunches is smaller[27] by a factor of 8.7. There is thus a room to increase the Ca^{17+} bunch intensity by this factor while preserving exactly the same $\Delta Q_{\rm SC}$. For the requisite bunch intensity for high-luminosity collisions, discussed in Section 4.3, the space-charge tune shift parameter would have to be higher by 70% with respect to its present value for the Pb^{54+} bunches. The beam cooling at the SPS could easily compensate this rise, provided that such bunches will survive the LEIR, PS and SPS acceleration phases. This aspect deserves more detailed studies and tests.

The magnetic rigidity of the Ca^{17+} beam is by a factor of 1.6 smaller, at the equivalent beam momentum, than for the Pb^{54+} beam. To preserve the beam optics in the transfer lines between the LEIR, PS and SPS rings, the injection energies per nucleon would have to be increased while switching from the Pb to Ca beams by a factor of $[(Z - N_e)_{\rm Ca} \times A_{\rm Pb}]/[(Z - N_e)_{\rm Pb} \times A_{\rm Ca}]$. An alternative approach, based on the same beam injection energies and changed magnetic field in the transfer lines, can also be employed but at the cost of increase of the space-charge tune shift parameter. Dedicated studies of the beam transfer aspects are needed to optimise the transfer of the $^{40}Ca^{17+}$ ions in the injector transfer lines.

7.3 Laser cooling at the SPS

7.3.1 Laser–Ca-beam collision parameters

The Ca^{17+}-beam cooling, proposed below, uses the atomic $2s$–$3p$ transition. The energy of the $2s$–$3p$ transition is 661.89 eV. For the optimal phase of cooling at the flat-top of the SPS acceleration cycle (just before the extraction to the LHC), the Lorentz factor of the beam should be $\gamma_L = 205$. The incoming laser-photon energy is $2\gamma_L$ times lower than the atomic excitation energy in its rest frame – at the top SPS energy it should be equal to 1.6 eV. The corresponding wavelength of the laser photons is 768 nm for the nearly

[27] We assume here that LEIR will operate the Ca^{17+} beam at the same magnetic rigidity as the Pb^{54+} beam.

head-on collision of the laser beam with the ion beam. The full set of parameters for the Ca^{17+}-beam cooling configuration in the SPS is summarised in Table 1.

Table 1: Parameters of the calcium-beam cooling configuration in the SPS.

Ion beam	$^{40}Ca^{17+}$
m – ion mass	37.21 GeV/c^2
E – mean energy	7.65 TeV
$\gamma_L = E/mc^2$– mean Lorentz relativistic factor	205.62
N – number ions per bunch	4×10^9
σ_E/E – RMS relative energy spread	2×10^{-4}
ϵ_n – normalised transverse emittance	1.5 mm mrad
σ_x – RMS transverse size	0.80 mm
σ_y – RMS transverse size	0.57 mm
σ_z – RMS bunch length	10 cm
Dispersion function	2.44 m
Laser	pulsed Ti:Sa (20MHz)
λ – wavelength ($\hbar\omega$ – photon energy)	768 nm (1.6 eV)
σ_λ/λ – RMS relative band spread	2×10^{-4}
U – single pulse energy at IP	2 mJ
σ_L – RMS transverse intensity distribution at IP ($\sigma_L = w_L/2$)	0.56 mm
σ_t – RMS pulse duration	2.04 ps
θ_L – collision angle	1.3 deg
Atomic transition of $^{40}Ca^{17+}$	$2s \rightarrow 3p$
$\hbar\omega_0'$ – resonance energy	661.89 eV
τ' – mean lifetime of spontaneous emission	0.4279 ps
$\hbar\omega_1^{\max}$ – maximum emitted photon energy	271 keV

The ion-beam parameters assume that the beam-cooling interaction point (IP) will be placed at the half-cell 627 of the SPS, in the place of the planned Gamma Factory PoP experiment [13]. A commercial Titanium:Sapphire mode-lock laser oscillator[28] , which provides excellent phase noise stability, fulfils the requisite requirements for the photon source. The effective photon flux is increased to its requisite value by using a high-gain Fabry–Pérot resonator with a typical enhancement factor of 10^4 [13, 84].

7.3.2 Simulation results

Monte Carlo turn-by-turn simulations of ion-bunch dynamics during the cooling process have been performed using the full-turn 6D transport matrix for the SPS lattice [85].

In order to couple the horizontal betatron oscillations to the vertical ones, the betatron tunes in the uncoupled case are set to the same value: $\nu_x = \nu_y = 26.13$ (while the design

[28]We are indebted to Kevin Cassou and Aurelien Martens for the numerous discussions and sharing with us their knowledge on the available laser technology.

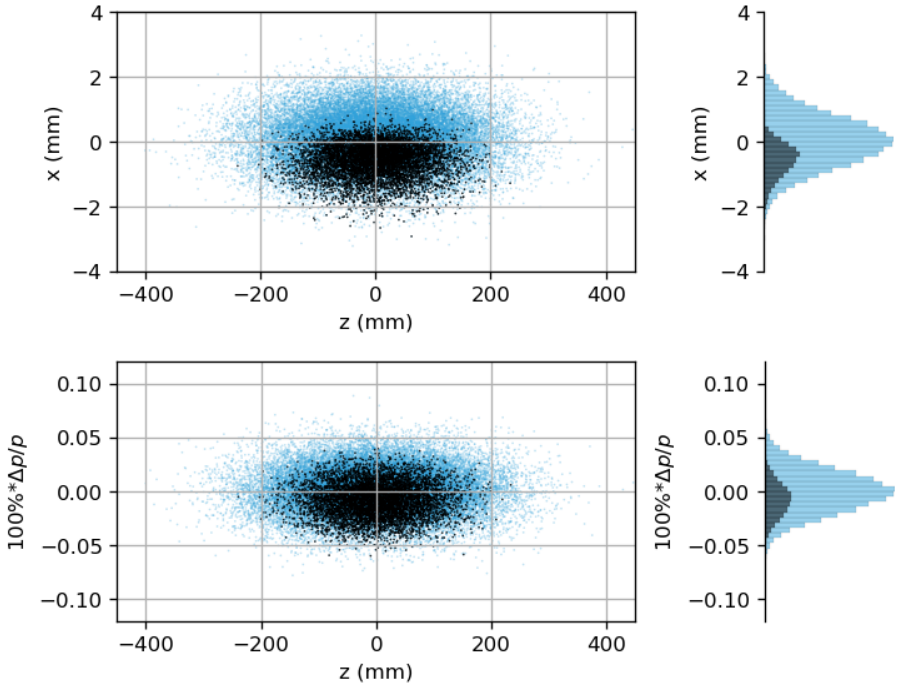

Figure 9: Distributions of the positions and momenta of the ions interacting with the pulse of the first laser. Excited ions are shown as black dots while non-excited ions are shown as blue dots. The shift of the laser pulse by $-1.4\,\mathrm{mm}$ provides an optimal coupling of horizontal betatron oscillations to synchrotron oscillations, as explained in Fig. 7. About 17% of all ions are excited in each bunch crossing.

values are only slightly different: $\nu_x = 26.13$, $\nu_y = 26.18$). In such a case, the transverse coupling is introduced with a single 1 m long skew-quadrupole with a strength which is approximately 10 times lower than the typical SPS quadrupole strength. The resulting width of the coupling resonance (tune separation) is 0.0078. This means that the vertical betatron oscillations are transferred into the horizontal oscillations in about 100 turns.

In order to couple the transverse oscillations to the synchrotron oscillations, the focal point of the first laser beam, of the 2 mJ pulse power, is shifted by 1.4 mm in the negative horizontal direction with respect to the ion-beam axis. The resulting distributions of the positions and momenta of the single-bunch ions which are excited by a single laser pulse are shown in Fig. 9. The number of the excited ions at $\Delta p < 0$, as shown in Fig. 9, is slightly larger than the number of the ions excited at $\Delta p > 0$. This leads to the longitudinal emittance blow-up, unless it is "corrected" with the second laser. This additional laser allows to counteract the longitudinal emittance blow-up induced by the transverse cooling. The focal point of its photon pulses is aligned, in the transverse plane, with the centre of the ion beam spot.

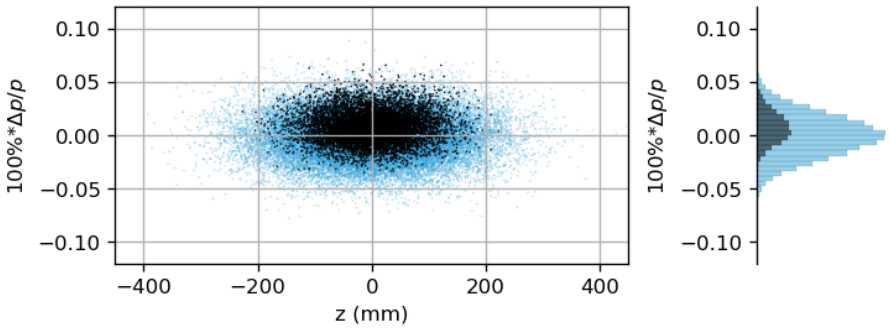

Figure 10: Distribution of the momentum and longitudinal positions of the ions interacting with the photon-pulse of the second laser. Excited ions are shown as black dots while non-excited ions are shown as blue dots. The laser pulse focal point is aligned with the ion beam centre but its frequency band is shifted to excite the higher-momentum ions, as explained in Fig. 6.

The frequency-band of the second laser is tuned to excite the ions predominantly in the upper part of their momentum distribution, as shown in Fig. 10. Its pulse power is two times smaller than that of the first one. This configuration assures stable transverse cooling while preserving the longitudinal bunch size. If the power of the second-laser pulse were increased, the ion-bunch length would be decreased. This regime is also interesting to be considered. However, it would require supplementary studies of the longitudinal stability of short ion bunches in the SPS. By keeping the longitudinal bunch size unchanged over the transverse beam cooling phase, the bunches are protected against longitudinal instabilities, e.g. the microwave instability, and the intra-beam scattering rate of the beam particles is reduced. The transverse stability [86–88] of the low-emittance ion beam in the SPS and LHC deserves complementary studies. They should involve investigations of the transverse mode coupling and head-tail instabilities.

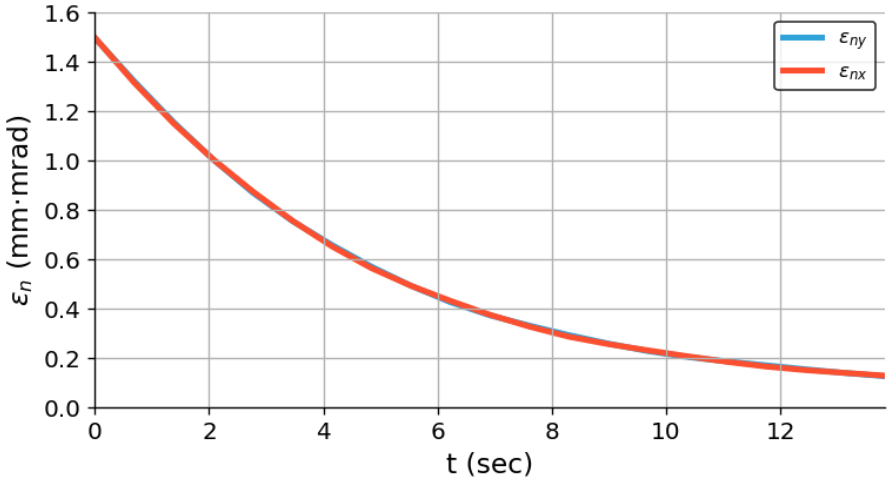

Figure 11: Transverse cooling speed: the time-evolution curves of the vertical and horizontal emittances are overlapping each other – they are precisely equal when the betatron tunes are on the coupling resonance.

The evolution of the transverse beam emittance in the proposed scheme is shown in Fig. 11. A factor of 3 reduction of the transverse emittance can be achieved in 5 seconds and a factor of 5 in 8 seconds.

7.4 Ca^{20+} beam in LHC

The three electrons remaining attached to the Ca nucleus over the beam cooling process in the SPS storage ring have to be stripped in the TI2 and TI8 transfer lines before accelerating the ion bunches in the LHC. Dedicated studies will be required to optimise the stripper material and thickness, such that the maximal Ca^{20+} transmission efficiency is associated with a negligible increase of the beam momentum dispersion, caused by the ion energy loss, and with the minimal emittance blow up, caused by multiple scattering of the ions in the stripper material. Optimisation of the position of the stripper may be needed for the present Twiss function of the transfer line (the stripper-induced emittance growth is minimal for placing the stripper at the the minimal beta point). Note that the above constraints are less critical than the corresponding constraints for the stripping of the Pb^{54+} ions in the PS to SPS TT2 line [89] because of: (1) significantly larger (by a factor of 30) ion-beam energy at the stripper position, (2) a smaller number (by a factor of 10) of electrons which need to be stripped off and (3) significantly smaller (reduced by a factor of $Z^2_{\rm Ca}/Z^2_{\rm Pb}$) binding energies of electrons. The latter two factors allow to reduce considerably the stripper thickness. According to initial estimates, the emittance blow-up in the stripper can be kept smaller than $\Delta\epsilon_n = 0.1\,\mathrm{mm\,mrad}$ and should not contribute to a sizeable emittance blow-up.

Another, more important, effect which would need to be studied is the effect of the blow-up of the beam transverse emittance over the phase of stacking the SPS batches into

the SPS ring and over the phase of the beam acceleration. The emittance blow-up is caused by the intra-beam scattering of the beam particles. Several techniques may be applied to counterbalance the corresponding emittance growth and, as a fallback solution, the stochastic cooling at the top beam-collision energy may need to be employed to mitigate the intra-beam scattering driven emittance growth.

Let us note that at the Relativistic Heavy Ion Collider (RHIC), the stochastic cooling of the bunched gold and uranium beams has been very successful [66–68]. The emittance growth was substantially reduced, improving the luminosity lifetime. For the uranium operation it was possible even to increase the instantaneous luminosity by more than a factor of 3 over its initial value. Such a method could also be exploited for the LHC ion beams [68]. Another fallback option would be to implement the optical stochastic cooling method, specially designed for the high-brightness beams [69]. Both methods could help in preserving the initial, LHC-injection phase, beam transverse emittance.

The optical stochastic cooling may turn to be necessary not only to reduce the intra-beam scattering emittance growth but also to be able run the collisions of the low-emittance beams with a high value of the beam–beam parameter. For the equivalent and maximal partonic luminosity, the beam–beam parameter in the CaCa collisions at the LHC would be significantly higher than that for the *pp* collisions. It would reach the value of $\xi_{x,y} \approx 0.1$, which is by a factor of 3 larger than the one at the Tevatron collider. Running such a collisions scheme is anything but easy. It may require beam cooling and/or the use of electron lenses[29].

Finally, an additional aspect, which will require dedicated studies, is the beam collimation for the fully stripped calcium beam in the LHC. The LHC beam collimation system was designed for the proton beam and the losses of the beam particle that are specific for the nuclear beams, such as the neutron losses – leading to a change of the magnetic rigidity of the beam particles – would need to be evaluated. The reduced emittance of the beam may be of help for the collimation of the high-intensity calcium beam in the LHC rings.

7.5 Luminosity of CaCa collisions

The reduction of the transverse beam emittance of the calcium beam, at the flat-top SPS energy, to the value of $\epsilon_n = 0.3\,\mathrm{mm\,mrad}$ can be achieved, according to our simulations, within the cooling time of 8 seconds.

Let us assume that the normalised transverse emittance can be preserved over the time of the LHC fill and ramp or that the emittance growth in the LHC can be (if necessary) compensated by the stochastic cooling at the top beam energy. According to the formula (4.3), by using the high-luminosity LHC *pp*-mode parameters and the bunch population of the calcium beam taken from [64], the predicted peak nucleon–nucleon luminosity (or equivalently the partonic luminosity) in the CaCa collision mode with the

[29]We are indebted to Frank Zimmermann for drawing our attention to this potentially important luminosity-limiting factor.

50 ns bunch interval is expected to be

$$L_{NN} = 4.2 \times 10^{34} \mathrm{s}^{-1} \mathrm{cm}^{-2}. \tag{7.1}$$

The expected number of collisions per bunch crossing is $\nu_{\mathrm{CaCa}} = 5.5$. Note that for the same partonic luminosity, the number of collisions in the *pp* running mode would be $\nu_{pp} = 702$ – too large to be accepted for efficient operation of the ATLAS and CMS detectors. For the CaCa collisions, the number of produced particles, assuming the "wounded-nucleon scaling" discussed in Section 3.11, is expected to be lower at this luminosity than those for the 50 ns *pp* running mode at the levelled luminosity of $L_{pp} = 2.5 \times 10^{34}$ $\mathrm{s}^{-1} \mathrm{cm}^{-2}$, and for the 25 ns mode with the twice higher levelled luminosity.

The expected beam transverse emittance growth at such a luminosity is of the order of 1–2 hours. The expected optical stochastic cooling time for for the Ca beam at the top energy (in its simplest scheme of passive cooling with no optical amplifier) is 1.5 hours. The optical stochastic cooling should thus allow to reach the equilibrium between the beam cooling and beam heating processes at the above luminosity[30].

8 Conclusions and outlook

We have argued that nuclear beams, and in particular isoscalar nuclear beams, have numerous advantages with respect to the proton beams for the high-luminosity phase of the LHC operation. They allow to make the full use of the isospin symmetry of the strong interactions in constraining the flavour and momentum distributions of their partonic degrees of freedom. As a consequence, the analysis of the SM EW and BSM processes becomes insensitive to the limited precision of the LHC-external constraints, which will always remain essential for the interpretation of the numerous *pp* collision measurements. The nuclear beams can serve as analysers (targets) to study the propagation asymmetries of the longitudinally and transversely polarised W and Z bosons in vacuum and matter. They can generate effective photon beams of unprecedented intensity, unreachable with the proton beams, opening the path to studies of the Higgs-boson production in photon–photon collisions. Finally, they reduce the pile-up background in the high-luminosity phase of LHC operation while preserving the same partonic luminosity or, conversely, increase the HL-LHC partonic luminosity at a fixed soft-particle pile-up level.

We have proposed a new operation scheme of nuclear beams which includes a significant reduction of their transverse emittance by laser cooling. This scheme creates a possibility to reach, for low-Z nuclear beams, a comparable partonic luminosity to that foreseen for the high-luminosity phase of *pp* collisions.

A concrete scenario for the calcium beams is presented and evaluated. In this scenario, the Ca^{17+} ion beam coming from the ion source is cooled at the SPS flat-top energy and its transverse emittance is reduced over the cooling time of 15 seconds to the value of $\epsilon_n = 0.3\,\mathrm{mm\,mrad}$. Assuming that the transverse emittance of such a beam is preserved

[30]We are indebted to Valeri Lebedev for his calculations of the optical stochastic cooling time for the calcium-ion beam.

over the phase of stacking of the SPS batches in the LHC and over its acceleration phase, the expected peak nucleon–nucleon (partonic) luminosity for the CaCa collisions is $L_{NN} = 4.2 \times 10^{34}\,\mathrm{s}^{-1}\mathrm{cm}^{-2}$. This value is higher than the levelled value for the high-luminosity pp collisions with 50 ns bunch spacing and similar to that for the 25 ns mode. This scenario deserves further studies. The most important aspects of such remaining studies have been identified and discussed.

The cold light-ion beams are, in our view, the best candidates to achieve the highest luminosity at the future high-energy hadron colliders, e.g. the FCC-hh. The cooling efficiency in the LHC (if used as a injector to the FCC-hh) will be higher w.r.t. the SPS. The LHC vacuum is by a factor of 1000 better than that of the SPS, and, most importantly, the blow up of the transverse beam emittance over the time interval between the beam-cooling phase and the beam-collision phase is significantly reduced due to increase of the Lorentz γ_L-factor of the beam. This is another reason why the proposed scheme should be considered seriously, elaborated in more details and allowed to be proven in the dedicated runs of the Gamma Factory Proof-of-Principle experiment at the SPS.

Acknowledgements

We would like to thank all the members of the Gamma Factory group for numerous discussions and encouragement. Particular thanks to: Reyes Allemany-Fernandez, Hannes Bartosik, Evgeny Bessonov, Roderick Bruce, Dima Budker, Kevin Cassou, Camilla Curatolo, Yann Dutheil, Brennan Goddard, John Jowett, Detlef Kuchler, Mike Lamont, Valeri Lebedev, Thibaud Lefevre, Aurelien Martens, Michaela Schaumann, Richard Scrivens, Slava Shevelko, Vladimir Shiltsev and Frank Zimmermann.

A. Petrenko acknowledges a personal grant from the Foundation for the Advancement of Theoretical Physics and Mathematics “BASIS”.

Appendices

A Parton distribution functions for protons and nuclei

Parton distribution functions (PDFs) were introduced by Feynman in 1969 to explain the Bjorken scaling in deep inelastic scattering data. They have interpretation of probability distributions of finding a given parton within a hadron or a nucleus with a longitudinal momentum fraction x of its parent at a resolution scale Q^2. Within QCD/QED the partons are interpreted as quarks, gluons and photons. According to the QCD factorisation theorem for inclusive hard-scattering processes, PDFs are universal distributions containing long-distance (non-perturbative) structure of hadrons/nuclei. They are key ingredients for phenomenology of high-energy hadron/nucleus collisions.

Since PDFs are non-perturbative objects, they cannot be calculated from first principles using perturbative QCD methods[31]. Instead, they are usually parametrised at some initial scale Q_0^2 with the help of a set of chosen parameter-dependent functions. Then, they are evolved to any scale $Q^2 > Q_0^2$ using the DGLAP equations [15] at a given order of perturbative QCD (LO, NLO, NNLO) and fitted to experimental data for the used parameters/functions. In this way an appropriate PDFs parametrisation is obtained and it is usually supplied with some uncertainties corresponding to 1σ errors of the respective likelihood analysis. Fits are performed for various kinds of data from deep inelastic lepton–nucleon/nucleus scattering as well as hadron–hadron, hadron–nucleus and nucleus–nucleus collision experiments in order to have as good as possible parton-flavour sensitivity and x-range coverage. Currently, there are several groups that provide independent PDFs parametrisations using different assumptions and/or analysis methods – for a recent review see e.g. Ref. [91].

The proton PDFs are known to a much better precision than the nuclear ones as they have been the main focus of phenomenology for the lepton–proton and proton–(anti)proton collider experiments over the last 50 years. In Table 2 we summarise theoretical, experimental and methodological features of the recent proton PDF parametrisation sets: CT18 [92], MMHT14 [93], NNPDF3.1 [94] and ABMP16 [95, 96]; based on Ref. [91]. The MMHT14 and NNPDF3.1 sets have been updated since their first publications, taking into account new experimental data and improving theoretical frameworks; for more details see e.g. Ref. [91]. Other proton PDF parametrisations currently available are JAM19 [97], JR14 [98], CJ15 [99] and HERAPDF2.0 [100], although they are based on smaller sets of measurements than the ones listed in Table 2.

The need for precise nuclear PDFs has been driven recently mainly by heavy-ion collisions at the LHC. A summary of the theoretical, experimental and methodological features of the recent nuclear PDF parametrisation sets nCTEQ15 [16], EPPS16 [101],

[31] There are attempts to obtain PDFs using non-perturbative techniques of lattice QCD, but such PDFs are still far from practical applications for the HEP phenomenology, see e.g. [90] and references therein.

Proton PDFs	CT18	MMHT14	NNPDF3.1	ABMP16
Perturbative order	NLO, NNLO	LO, NLO, NNLO	LO, NLO, NNLO	NLO, NNLO
Heavy-quark scheme	S-ACOT	optimal-TR	FONLL	FFN
Value of $\alpha_s(m_Z)$	0.118	0.118	0.118	fitted
Input scale Q_0	1.30 GeV	1.00 GeV	1.65 GeV	3.00 GeV
Fixed Target DIS	✓	✓	✓	✓
Collider DIS	✓	✓	✓	✓
Fixed Target SIDIS				✓
Fixed Target DY	✓	✓	✓	✓
Collider DY	✓	✓	✓	✓
Jet production	✓	✓	✓	✓
Top production	$t\bar{t}$ tot., diff.	$t\bar{t}$ tot.	$t\bar{t}$ tot., diff.	$t\bar{t}$, single-t, tot.
Independent PDFs	6	7	8	6
Parameterisation	Bernstein pol.	Chebyshev pol.	neural network	simple pol.
Free parameters	29	37	296	25
Statistical tretment	Hessian	Hessian	Monte Carlo	Hessian
Tolerance	$\Delta\chi^2 = 100$	$\Delta\chi^2$ dynamical	n/a	$\Delta\chi^2 = 1$

Table 2: Theoretical, experimental and methodological features of some recent proton PDF sets, from Ref. [91].

Nuclear PDFs	nCTEQ15	EPPS16	nNNPDF1.0	TUJU19
Perturbative order	NLO	NLO	NLO, NNLO	NLO, NNLO
Heavy quark scheme	ACOT	S-ACOT	FONLL	ZM-VFN
Value of $\alpha_s(m_Z)$	0.118	0.118	0.118	0.118
Input scale Q_0	1.30 GeV	1.30 GeV	1.00 GeV	1.30 GeV
Fixed Target DIS	✓	✓	(w/o ν-DIS)	✓
Fixed Target DY	✓	✓		
Colider DY		✓		
Jet and had. prod.	(π^0 only)	(π^0, dijet)		
Independent PDFs	6	6	3	6
Parameterisation	simple pol.	simple pol.	neural network	simple pol.
Free parameters	16	20	178	16
Statistical treatment	Hessian	Hessian	Monte Carlo	Hessian
Tolerance	$\Delta\chi^2 = 35$	$\Delta\chi^2 = 52$	n/a	$\Delta\chi^2 = 50$

Table 3: Theoretical, experimental and methodological features of the recent nuclear PDF sets, from Ref. [91].

nNNPDF1.0 [102] and TUJU19 [103] is presented in Table 3; based on Ref. [91]. The nCTEQ15 and EPPS16 sets have been updated since their original publications with some new experimental data, for more details see e.g. Ref. [91]. The nuclear PDFs are usually provided in terms of the correction factors $R_i^A(x, Q^2)$ with respect to the proton PDFs, as given by Eqs. (2.4) and (2.5) when integrated over k_t. The present precision of nuclear PDFs is significantly worse that the proton PDFs. Most of the above proton and nuclear PDF sets are publicly avaliable through the LHAPDF library [104].

The advantage of the PDFs is that they are universal and can be combined with theoretical perturbative calculations for any hard parton-level process in high-energy lepton–hadron/nucleus and hadron/nucleus–hadron/nucleus collisions. For many Standard Model processes at the LHC, these theoretical predictions are given at the next-to-next-to-leading (NNLO) accuracy in the strong coupling constant α_s. These PDFs have, however, an important drawback – they are integrated over the transverse degrees of freedom of the respective partons, so they do not provide any information on the distributions of their transverse momenta k_t. Many observables at the LHC are sensitive to the transverse momenta of initial partons, in particular to their intrinsic (non-perturbative) k_t. This is particularly important for precision measurements of the Standard Model parameters, such as the W-boson mass and the weak-mixing angle. This is the reason why, in Section 2 we have not referred to these "collinear" PDFs but used a more general notion of partonic distributions that depend on both x and k_t.

In general, transverse-momentum-dependent (TMD), or "unintegrated", PDFs, contrary to the above collinear PFDs, are not process independent, see e.g. [105]. However, they can be defined unambiguously for specific high-energy scattering processes, such as semi-inclusive deep-inelastic scattering (SIDIS), the Drell–Yann process, the Higgs-boson production in pp collisions, see e.g. Refs. [106–108]. Some parametrisation sets of this kind of TMD PDFs for protons and lead nuclei are publicly available through the TMDlib library [109, 110].

B Photon absorption and emission by ultra-relativistic partially stripped ions

B.1 Kinematics

Interaction of photons with ultra-relativistic partially stripped ions is the key phenomenon which drives the beam-cooling process. Let us consider counter-propagating beams of laser photons and ions. Due to the relativistic Doppler shift, the energy of the laser photons is boosted in the ion rest frame proportionally to the Lorenz γ_L-factor of the ion beam. If tuned to atomic transition energy of the ions, the laser photons are resonantly absorbed with a large (gigabarn-level) cross section. Excited ions eventually decay into their ground state by emitting photons. This process is shown in Fig. 12. For the ultra-

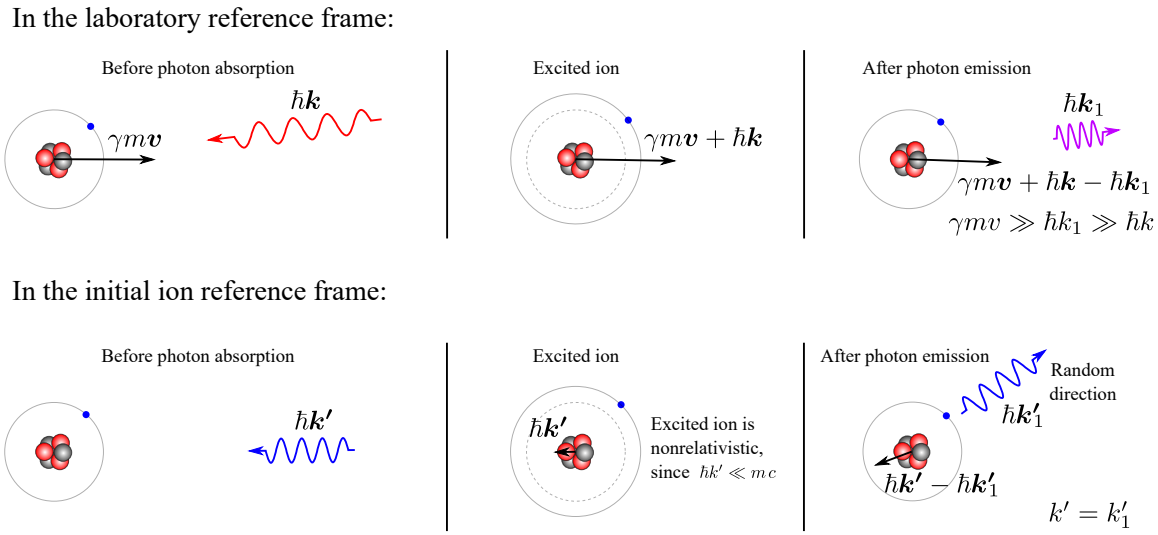

Figure 12: The process of photon scattering in the laboratory and ion-rest reference frames.

relativistic ions, this absorption and emission scheme enables a conversion of infra-red, visible or near-ultraviolet photons into X-ray or γ-ray photons.

To describe this process quantitatively, we use 4-vectors $(E/c, \boldsymbol{p})$. The Lorentz transformation of these 4-vectors, for the z-axis aligned with the direction of the ion motion, can be written as

$$\begin{pmatrix} E'/c \\ p'_x \\ p'_y \\ p'_z \end{pmatrix} = \begin{pmatrix} \gamma_L & 0 & 0 & -\beta\gamma_L \\ 0 & 1 & 0 & 0 \\ 0 & 0 & 1 & 0 \\ -\beta\gamma_L & 0 & 0 & \gamma_L \end{pmatrix} \begin{pmatrix} E/c \\ p_x \\ p_y \\ p_z \end{pmatrix}, \tag{B.1}$$

where the primed 4-vector components correspond to the ion-rest frame (Fig. 13).

The ion 4-momentum is denoted, in the following, by $(\gamma_L mc, \gamma_L m\boldsymbol{v})$ and the photon 4-momentum by $(\hbar\omega/c, \hbar\boldsymbol{k})$. Since the photon momentum $\boldsymbol{p}$ is related to the light's wave-

vector $\boldsymbol{k}$ through $\boldsymbol{p} = \hbar\boldsymbol{k}$, where $\hbar$ is the reduced Planck constant, $k_x = -k\sin\theta$, $k_y = 0$, $k_z = -k\cos\theta$, and $k = \omega/c$, one can rewrite Eq. (B.1) as follows:

$$\begin{pmatrix} 1 \\ -\sin\theta' \\ 0 \\ -\cos\theta' \end{pmatrix} \omega' = \begin{pmatrix} \gamma_L & 0 & 0 & -\beta\gamma_L \\ 0 & 1 & 0 & 0 \\ 0 & 0 & 1 & 0 \\ -\beta\gamma_L & 0 & 0 & \gamma_L \end{pmatrix} \begin{pmatrix} 1 \\ -\sin\theta \\ 0 \\ -\cos\theta \end{pmatrix} \omega. \tag{B.2}$$

The relation between the photon frequency in the two frames is given by

$$\omega' = (1 + \beta\cos\theta)\gamma_L\omega \approx \left(1 + \beta - \beta\frac{\theta^2}{2}\right)\gamma_L\omega \approx 2\gamma_L\omega. \tag{B.3}$$

Eq. (B.3) shows that the frequency of the photon in the ion-rest frame is $2\gamma_L$-times larger than in the laboratory frame. Such photons can excite transitions which are inaccessible for the stationary ions.

Tuning of the photon frequencies to the resonant atomic transitions requires a precise control of the ion-beam angular divergence and its momentum spread. The angular divergence of the ion beam, $\Delta\theta$, may have an impact on the frequency (energy) spread of the photons in the ion rest frame. However, since

$$\omega' \sin\theta' = \omega \sin\theta, \tag{B.4}$$

the spread

$$\Delta\theta' \approx \frac{\Delta\theta}{2\gamma_L}, \tag{B.5}$$

is significantly suppressed in the ion-rest frame, as depicted in Fig. 13. For example, the

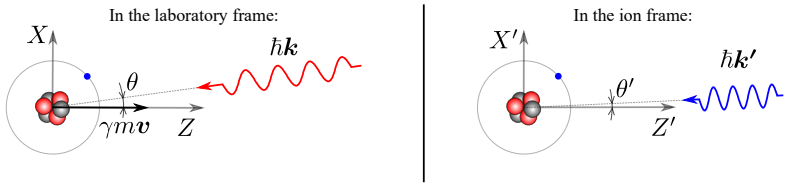

Figure 13: Photon absorption kinamatics in the laboratory and ion-rest frames.

spread of the order of $\Delta\theta \approx 1\,\text{mrad}$ corresponds to the ion-frame frequency spread of only $\sim 10^{-6}$. This shows that the angular divergence of the ion beam does not contribute significantly to the effective photon-energy spread. A significantly more important contribution comes from the energy spread in the ion beam (typically $\Delta\gamma_L/\gamma_L \approx 10^{-4}$). In order to achieve a high excitation rate of the ion beam, the frequency spread of the laser pulse should be tuned to be comparable to the ion-beam energy spread.

The process of emission of a photon is depicted in Fig. 14, both in the laboratory and the ion-rest frame. For the atomic transitions considered in this paper as candidates for the beam cooling process, photons are emitted isotropically in the ion-rest frame.

Excited ion after the photon absorption:

Ion after the photon emission:

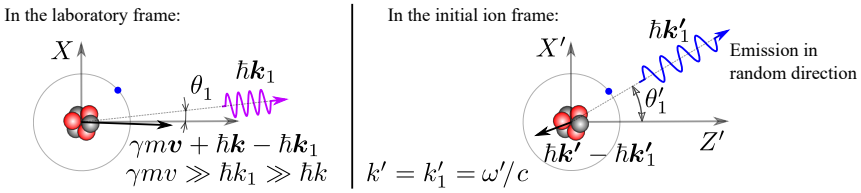

Figure 14: The excited ion after the photon absorption and the ion after the photon emission.

Their angular distribution is, however, strongly modified in the laboratory frame. Let us consider the process where the photon is emitted in the same plane as the absorbed laser photon (the x'–z' plane) at a random angle θ'_1. In such a case, the photon 4-vector components are given by $k'_{1x} = k' \sin\theta'_1$ and $k'_{1z} = k' \cos\theta'_1$, and the inverse Lorentz transformation describes the relation between the emitted-photon parameters in the two frames:

$$\begin{pmatrix} 1 \\ \sin\theta_1 \\ 0 \\ \cos\theta_1 \end{pmatrix} \omega_1 = \begin{pmatrix} \gamma_L & 0 & 0 & \beta\gamma_L \\ 0 & 1 & 0 & 0 \\ 0 & 0 & 1 & 0 \\ \beta\gamma_L & 0 & 0 & \gamma_L \end{pmatrix} \begin{pmatrix} 1 \\ \sin\theta'_1 \\ 0 \\ \cos\theta'_1 \end{pmatrix} \omega'. \tag{B.6}$$

The emitted photon frequency is given by:

$$\omega_1 = \gamma_L(1 + \beta\cos\theta'_1)\,\omega' \approx 2\gamma_L^2(1 + \beta\cos\theta'_1)\,\omega. \tag{B.7}$$

The laboratory-frame emission angle θ_1 can be also calculated using the inverse Lorentz transformation:

$$\omega_1 \sin\theta_1 = \omega' \sin\theta'_1 \;\Rightarrow\; \sin\theta_1 = \frac{\sin\theta'_1}{\gamma_L(1 + \beta\cos\theta'_1)}. \tag{B.8}$$

The resulting angular divergence of the emitted photons in the laboratory frame is small for highly relativistic ions: $\Delta\theta_1 \sim 1/\gamma_L$.

The change of the ratio of transverse to longitudinal momentum of the ion, due to the photon emission, is very small compared to the typical angular spread in the ion beam. Therefore, the main effect of the photon emission on the ion motion is the small loss of the ion total momentum.

B.2 Cross section

The cross section of the ion excitation by a photon with the frequency ω' [111, 112] can be written as

$$\sigma = 2\pi^2 c r_e f_{12} g(\omega' - \omega_0'), \tag{B.9}$$

where r_e is classical electron radius, f_{12} is the oscillator strength, ω_0' is the resonance frequency of the ion transition and $g(\omega' - \omega_0')$ is the Lorentzian function:

$$g(\omega' - \omega_0') = \frac{1}{2\pi} \frac{\Gamma}{(\omega' - \omega_0')^2 + \Gamma^2/4}\,, \tag{B.10}$$

where Γ is the atomic-resonance width related to the lifetime of the excited ion τ':

$$\Gamma = \frac{1}{\tau'}\,. \tag{B.11}$$

The atomic-resonance width can be expressed as

$$\Gamma = 2 r_e \omega_0'^2 f_{12} \frac{g_1}{c g_2}, \tag{B.12}$$

where g_1, g_2 are the degeneracy factors of the ground state and excited states, respectively.

The formula (B.9) can thus be rewitten in a simpler form:

$$\sigma(\omega' - \omega_0') = \frac{\sigma_0}{1 + 4\tau'^2(\omega' - \omega_0')^2}, \tag{B.13}$$

where

$$\sigma_0 = \frac{\lambda_0'^2 g_2}{2\pi g_1}, \tag{B.14}$$

and $\lambda_0' = 2\pi c/\omega_0'$ is the emitted photon wavelength.

Equations presented in this Appendix are used in the simulations of the beam cooling process presented in Section 7.3.

References

[1] M.W. Krasny, *The Gamma Factory proposal for CERN*, arXiv:1511.07794 [hep-ex].

[2] J.P. Berge *et al.*, Z. Phys. C **49** (1991) 187. doi:10.1007/BF01555493

[3] P.S. Auchincloss *et al.*, Z. Phys. C **48**, 411 (1990). doi:10.1007/BF01572022

[4] M. Tzanov *et al.* [NuTeV Collaboration], Phys. Rev. D **74** (2006) 012008, doi:10.1103/PhysRevD.74.012008 [hep-ex/0509010].

[5] P. Bosted *et al.*, AIP Conf. Proc. **176** (1988) 508, doi:10.1063/1.37683.

[6] J.V. Allaby *et al.* [CHARM Collaboration], Z. Phys. C **38** (1988) 403, doi:10.1007/BF01584388.

[7] M.W. Krasny, *Electron-Deuteron scattering at HERA*, in: Future Physics at HERA Proceedings of the DESY workshop 1995/96, Editors: G. Ingelman, A. De Roeck, R. Klanner.

[8] M.W. Krasny, F. Dydak, R. Voss, CERN-LHCC-2009-014 / LHCC-I-017, 17/09/2009.

[9] S. Schroder *et al.*, Phys. Rev. Lett. **64** (1990) 2901, doi:10.1103/PhysRevLett.64.2901.

[10] J.S. Hangst, M. Kristensen, J.S. Nielsen, O. Poulsen, J.P. Schiffer and P. Shi, Phys. Rev. Lett. **67** (1991) 1238, doi:10.1103/PhysRevLett.67.1238.

[11] I. Lauer *et al.*, Phys. Rev. Lett. **81** (1998) 2052, doi:10.1103/PhysRevLett.81.2052.

[12] M.W. Krasny [Gamma Factory Study Group], PoS **EPS-HEP2017** (2017) 532. doi:10.22323/1.314.0532

[13] M.W. Krasny *et al.* [Gamma Factory Study Group], *Gamma Factory Proof-of-Principle Experiment*, Letter of Intent, CERN-SPSC-2019-031/SPSC-I-253, 25/09/2019.

[14] K.J. Eskola, P. Paakkinen, H. Paukkunen and C.A. Salgado, PoS DIS **2017** (2018) 197, doi:10.22323/1.297.0197 [arXiv:1709.08347 [hep-ph]].

[15] V.N. Gribov and L.N. Lipatov, Sov. J. Nucl. Phys. **15** (1972) 438; L.N. Lipatov, Sov. J. Nucl. Phys. **20** (1975) 95; G. Altarelli and G. Parisi, Nucl. Phys. **126** (1977) 298; Yu.L. Dokshitzer, Sov. Phys. JETP **46** (1977) 64.

[16] K. Kovarik *et al.*, Phys. Rev. D **93** (2016) no.8, 085037, doi:10.1103/PhysRevD.93.085037 [arXiv:1509.00792 [hep-ph]].

[17] M.W. Krasny, *Everything you've always wanted to know about nuclei at HERA but you were afraid to ask*, summary talk at the "Future HERA Physics Workshop", Hamburg, June, 1996.

[18] M.W. Krasny, *Future HERA program, a memorandum to DESY directors B. Wiik and A. Wagner*, Hamburg, 11 July 1996.

[19] M. Arneodo, A. Bialas, M.W. Krasny, T. Sloan and M. Strikman, *Nuclear beams in HERA*, in: *Hamburg 1995/96, Future physics at HERA*, 887–926 [hep-ph/9610423].

[20] M.W. Krasny, Nucl. Phys. A **622** (1997) 95C. doi:10.1016/S0375-9474(97)00335-7.

[21] M.W. Krasny, *The nuclear experimental program for HERA*, "DESY/GSI/NUPECC workshop", Seeheim, Germany, March 1997.

[22] M.W. Krasny, *Electron-nucleus Collisions Future Experimental Program And New Challenges For QCD*, Proceedings of 34th Rencontres de Moriond on QCD and High Energy Hadronic Interactions: Les Arcs, France, Mar 20-27, 1999, J. Tran Thanh Van (ed.).

[23] M.W. Krasny, 1. *Physics of eA at eRHIC.* 2. *A Detector design for eRHIC.* Plenary talks at the "First eRHIC workshop on eA and polarised ep Collider Physics", Yale (New Heaven), USA, April 2000, Nucl. Phys. A **663** (2000) 56, doi:10.1016/S0375-9474(99)00572-2 [hep-ph/9907410].

[24] M.W. Krasny, *Physics with lepton-proton and lepton-ion collider*, overview talk presented at the "Snowmass workshop on the future of High Energy Physics", Snowmass, Colorado, USA, July 2001.

[25] M.W. Krasny, *Detector design issues for a generic QCD facility*, overview talk presented at the "Snowmass workshop on the future of High Energy Physics", Snowmass, Colorado, USA, July 2001.

[26] M.W. Krasny, Nucl. Phys. Proc. Suppl. **105** (2002) 185, doi:10.1016/S0920-5632(01)01978-8 [hep-ex/0110043].

[27] R. Holt *et al.*, *The Electron-Ion Collider. A high-luminosity probe of of the partonic substructure of nucleons and nuclei*, BNL Report 68933, February 2002.

[28] G. Bollen, AIP Conf. Proc. **1224** (2010) no.1, 432 doi:10.1063/1.3431449

[29] A. Accardi *et al.*, Eur. Phys. J. A **52** (2016) no.9, 268, doi:10.1140/epja/i2016-16268-9 [arXiv:1212.1701 [nucl-ex]].

[30] M.W. Krasny, F. Dydak, F. Fayette, W. Placzek and A. Siodmok, Eur. Phys. J. C **69** (2010) 379, doi:10.1140/epjc/s10052-010-1417-0 [arXiv:1004.2597 [hep-ex]].

[31] F. Fayette, M.W. Krasny, W. Placzek and A. Siodmok, Eur. Phys. J. C **63** (2009) 33, doi:10.1140/epjc/s10052-009-1084-1 [arXiv:0812.2571 [hep-ph]].

[32] M.W. Krasny *et al.*, *Generic analysis of Large ET Processes in Electron-Proton Scattering at HERA*, DESY, H1-Note, **H1-06/97-523**, (1997).

[33] M.W. Krasny, F. Fayette, W. Placzek and A. Siodmok, Eur. Phys. J. C **51** (2007) 607, doi:10.1140/epjc/s10052-007-0321-8 [hep-ph/0702251].

[34] D. Stump *et al.*, JHEP **10**, 046 (2003) []hep-ph/0303013].

[35] J. Pumplin *et al.*, JHEP **07**, 012 (2002) [hep-ph/0201195].

[36] M. Tanabashi *et al.* [Particle Data Group], Phys. Rev. D **98** (2018) no.3, 030001, and 2019 update, doi:10.1103/PhysRevD.98.030001.

[37] S. Schael *et al.* [ALEPH and DELPHI and L3 and OPAL and SLD Collaborations and LEP Electroweak Working Group and SLD Electroweak Group and SLD Heavy Flavour Group], Phys. Rept. **427** (2006) 257, doi:10.1016/j.physrep.2005.12.006 [hep-ex/0509008].

[38] S. Schael *et al.* [ALEPH and DELPHI and L3 and OPAL and LEP Electroweak Collaborations], Phys. Rept. **532** (2013) 119, doi:10.1016/j.physrep.2013.07.004 [arXiv:1302.3415 [hep-ex]].

[39] The ATLAS collaboration [ATLAS Collaboration], *Measurement of the effective leptonic weak mixing angle using electron and muon pairs from Z-boson decay in the ATLAS experiment at* $\sqrt{s} = 8$ *TeV*, ATLAS-CONF-2018-037.

[40] A. M. Sirunyan *et al.* [CMS Collaboration], Eur. Phys. J. C **78** (2018) no.9, 701, doi:10.1140/epjc/s10052-018-6148-7 [arXiv:1806.00863 [hep-ex]].

[41] R. Aaij *et al.* [LHCb Collaboration], JHEP **1511** (2015) 190, doi:10.1007/JHEP11(2015)190 [arXiv:1509.07645 [hep-ex]].

[42] The ATLAS collaboration, *Prospect for a measurement of the Weak Mixing Angle in* $pp \to Z/\gamma^* \to e^+e^-$ *events with the ATLAS detector at the High Luminosity Large Hadron Collider*, ATL-PHYS-PUB-2018-037, November 28, 2018.

[43] The CMS collaboration, *A proposal for the measurement of the weak mixing angle at the HL-LHC*, CMS Analysis Summary, CMS PAS FTR-17-001, December 1, 2017.

[44] The LHCb collaboration, *Prospects for measurement of the weak mixing angle at LHCb*, LHCb-PUB-2018-013, December 13, 2018.

[45] M. Aaboud *et al.* [ATLAS Collaboration], Eur. Phys. J. C **78** (2018) no.2, 110, Erratum: [Eur. Phys. J. C **78** (2018) no.11, 898], doi:10.1140/epjc/s10052-018-6354-3, 10.1140/epjc/s10052-017-5475-4 [arXiv:1701.07240 [hep-ex]].

[46] M.W. Krasny, S. Jadach and W. Placzek, Eur. Phys. J. C **44** (2005) 333, doi:10.1140/epjc/s2005-02398-2 [hep-ph/0503215].

[47] M.W. Krasny, J. Chwastowski and K. Slowikowski, Nucl. Instrum. Meth. A **584** (2008) 42 doi:10.1016/j.nima.2007.10.019 [hep-ex/0610052].

[48] M.W. Krasny, J. Chwastowski, A. Cyz and K. Slowikowski, Nucl. Instrum. Meth. A **729** (2013) 949 doi:10.1016/j.nima.2013.02.048 [arXiv:1006.3858 [physics.ins-det]].

[49] M.W. Krasny, J. Chwastowski, A. Cyz and K. Slowikowski, Nucl. Instrum. Meth. A **729** (2013) 934 doi:10.1016/j.nima.2013.07.070 [arXiv:1111.5851 [hep-ex]].

[50] G. Baur, K. Hencken, D. Trautmann, S. Sadovsky and Y. Kharlov, Phys. Rept. **364** (2002) 359, doi:10.1016/S0370-1573(01)00101-6 [hep-ph/0112211].

[51] D. d'Enterria, D.E. Martins and P. Rebello Teles, *Higgs boson production in photon-photon interactions with proton, light-ion, and heavy-ion beams at current and future colliders*, arXiv:1904.11936 [hep-ph].

[52] H. Paukkunen, PoS **HardProbes2018** (2018) 014, doi:10.22323/1.345.0014 [arXiv:1811.01976 [hep-ph]].

[53] E. Reya and A. Vogt, Z. Phys. C **67** (1995) 433.

[54] H. Paukkunen, Phys. Lett. B **745** (2015), 73, doi:10.1016/j.physletb.2015.04.037 [arXiv:1503.02448 [hep-ph]].

[55] G. Apollinari, O. Brüning, T. Nakamoto and L. Rossi, *High Luminosity Large Hadron Collider HL-LHC*, CERN Yellow Report (2015) no. 5, 1, doi:10.5170/CERN-2015-005.1 [arXiv:1705.08830 [physics.acc-ph]].

[56] M.L. Miller, K. Reygers, S.J. Sanders and P. Steinberg, Ann. Rev. Nucl. Part. Sci. **57** (2007) 205, doi:10.1146/annurev.nucl.57.090506.123020 [nucl-ex/0701025].

[57] A. Bialas, Acta Phys. Polon. B **43** (2012) 95, Erratum: [Acta Phys. Polon. B **43** (2012) 485], doi:10.5506/APhysPolB.43.485, 10.5506/APhysPolB.43.95 [arXiv:1202.4599 [hep-ph]].

[58] V. Shiltsev and F. Zimmermann, *Modern and Future Colliders*, arXiv:2003.09084 [physics.acc-ph], submitted to Rev. Mod. Phys.

[59] J. Stovall *et al.*, *On the Feasibility of Accelerating Deuterons in Linac4*, CERN-sLHC-Project-Note-0032 (2011).

[60] L. Arnaudon *et al.*, *Linac4 technical design report*, CERN-AB-2006-084.

[61] S. Benedetti, G. Bellodi, J. Lallement and A. Lombardi, *Redesign of CERN Linac3 RFQ for Lead 29+*, doi:10.18429/JACoW-LINAC2018-THPO057.

[62] J. Abelleira Fernandez *et al.*, *A Large Hadron Electron Collider at CERN*, [arXiv:1211.4831 [hep-ex]].

[63] C. Hill, D. Kuchler, R. Scrivens and F. Wenander, Rev. Sci. Instrum. **73** (2002) 564–566; doi:10.1063/1.1430033.

[64] Z. Citron *et al.*, *Report from Working Group 5 : Future physics opportunities for high-density QCD at the LHC with heavy-ion and proton beams*, CERN Yellow Rep. Monogr. (2019) 1159, doi:10.23731/CYRM-2019-007.1159 [arXiv:1812.06772 [hep-ph]].

[65] M.W. Krasny, Nucl. Instrum. Meth. A **540** (2005) 222, doi:10.1016/j.nima.2004.11.022 [hep-ex/0405028].

[66] M. Blaskiewicz and J.M. Brennan, Phys. Rev. ST Accel. Beams **10** (2007) 061001, doi:10.1103/PhysRevSTAB.10.061001.

[67] M. Blaskiewicz, J.M. Brennan and F. Severino, Phys. Rev. Lett. **100** (2008) 174802, doi:10.1103/PhysRevLett.100.174802.

[68] M. Schaumann, J.M. Jowett, B. Salvant, M. Wendt, M. Blaskiewicz and S. Verdú-Andrés, *Studies on Stochastic Cooling of Heavy Ions in the LHC*, doi:10.18429/JACoW-IPAC2014-TUPRO013.

[69] V. Lebedev, *Optical Stochastic Cooling*, ICFA Beam Dyn. Newslett. **65** (2014) 100.

[70] D. Winters *et al.*, Phys. Scripta T **166** (2015) 014048, doi:10.1088/0031-8949/2015/T166/014048.

[71] E.G. Bessonov and K.J. Kim, Phys. Rev. Lett., 76, p. 431–434 (1996).

[72] E. G. Bessonov and R.M. Feshchenko, *Stimulated Radiation Cooling*, Proceedings of RuPAC 2008, Zvenigorod, Russia.

[73] I. Lauer *et al.*, Phys. Rev. Lett., 81, p. 2052–2055 (1998).

[74] J. Jowett, B. Auchmann, C. Bahamonde Castro, M. Kalliokoski, A. Lechner, T. Mertens, M. Schaumann and C. Xu, *Bound-Free Pair Production in LHC Pb–Pb Operation at 6.37 Z TeV per Beam*, doi:10.18429/JACoW-IPAC2016-TUPMW028.

[75] D. Brandt, K. Eggert and A. Morsch, *Luminosity considerations for different ion species*, CERN-AT-94-05-DI, CERN-SL-94-04-AP, CERN-LHC-NOTE-264.

[76] N. Winckler, A. Rybalchenko, V.P. Shevelko, M. Al-Turany, T. Kollegger and T. Stöhlker, Nucl. Instrum. Meth. B **392** (2017) 67, doi:10.1016/j.nimb.2016.11.035.

[77] S. Hirlaender *et al.*, *Lifetime and Beam Losses Studies of Partially Strip Ions in the SPS ($^{129}Xe^{39+}$)*, Proceedings, 9th International Particle Accelerator Conference IPAC 2018, Vancouver, BC Canada, 2018.

[78] *Xenon beams light path to gamma factory*, `https://cerncourier.com/xenon-beams-light-path-to-gamma-factory/`, November 2017, p. 7.

[79] S. Charley, *LHC accelerates its first "atoms"*, `home.cern/news/news/accelerators/lhc-accelerates-its-first-atoms`.

[80] M. Schaumann *et al.*, *First partially stripped ions in the LHC ($^{208}Pb^{81+}$)*, doi:10.18429/JACoW-IPAC2019-MOPRB055, 10.1088/1742-6596/1350/1/012071.

[81] Bernhard Wolf, *Handbook of ion sources*, CRC Press, 1995.

[82] E. Baron, M. Bajard and Ch. Ricaud, *Charge exchange of very heavy ions in carbon foils and in the residual gas of GANIL cyclotrons*, Nuclear Instruments and Methods in Physics Research Section A: Accelerators, Spectrometers, Detectors and Associated Equipment, 328, (1993) 177.

[83] G. Schiwietz and P. Grande, *Improved charge-state formulas*, Nuclear Instruments and Methods in Physics Research Section B: Beam Interactions with Materials and Atoms, 175 (2001) 125.

[84] A. Börzsönyi *et al.*, Appl. Opt. **52** (2013) 8376, doi:10.1364/AO.52.008376

[85] A. Petrenko, *Python notebook simulating the dynamics of* Li-*like* Ca *beam cooling in the SPS*, `https://anaconda.org/petrenko/li_like_ca_in_sps_transv`, 2020.

[86] H. Bartosik, G. Iadarola, Y. Papaphilippou, G. Rumolo, B. Salvant and C. Zannini, doi:10.18429/JACoW-IPAC2014-TUPME026

[87] C. Zannini, H. Bartosik, G. Iadarola, G. Rumolo and B. Salvant, doi:10.18429/JACoW-IPAC2015-MOPJE049

[88] M. Carlà *et al.*, *Transverse beam dynamics studies with high intensity LHC beams in the SPS*, doi:10.18429/JACoW-IPAC2019-MOPTS089

[89] G. Arduini *et al.*, *Lead ion beam emittance and transmission studies in the PS – SPS complex at CERN*, Conf. Proc. C **960610** (1996) 380.

[90] Y. Liu *et al.* [Lattice Parton], Phys. Rev. D **101** (2020) no. 3, 034020, doi:10.1103/PhysRevD.101.034020 [arXiv:1807.06566 [hep-lat]].

[91] J.J. Ethier and E.R. Nocera, Ann. Rev. Nucl. PartSci. (2020) no. 70, 1–34, doi:10.1146/annurev-nucl-011720-042725 [arXiv:2001.07722 [hep-ph]].

[92] T.J. Hou *et al.*, arXiv:1912.10053 [hep-ph] (2019).

[93] L.A. Harland-Lang, A.D. Martin, P. Motylinski and R.S. Thorne, Eur. Phys. J. C **75** (2015) 204.

[94] R.D. Ball em et al., Eur. Phys. J. C **77** (2017) 663.

[95] S. Alekhin, J. Blümlein, S. Moch and R. Placakyte, Phys. Rev. D **96** (2017) 014011.

[96] S. Alekhin, J. Blümlein, S. Moch. Eur. Phys. J. C **78** (2018) 477.

[97] N. Sato, C. Andres, J.J. Ethier and W. Melnitchouk, arXiv:1905.03788 [hep-ph] (2019).

[98] P. Jimenez-Delgado and E. Reya, Phys. Rev. D **89** (2014) 074049.

[99] A. Accardi *et al.*, Phys. Rev. D **93** (2016) 114017.

[100] H. Abramowicz *et al.*, Eur. Phys. J. C **75** (2015) 580.

[101] K.J. Eskola, P. Paakkinen, H. Paukkunen and C.A. Salgado, Eur. Phys. J. C **77** (2017) 163.

[102] R. Abdul Khalek, J.J. Ethier and J. Rojo, Eur. Phys. J. C **79** (2019) 471.

[103] M. Walt, I. Helenius and W. Vogelsang, Phys. Rev. D **100** (2019) 096015.

[104] A. Buckley *et al.*, Eur. Phys. J. C **75** (2015) 132.

[105] E. Avsar, Int. J. Mod. Phys. Conf. Ser. **04** (2011), 74-84 doi:10.1142/S2010194511001589 [arXiv:1108.1181 [hep-ph]].

[106] R. Angeles-Martinez *et al.*, Acta Phys. Polon. B **46** (2015) no.12, 2501-2534 doi:10.5506/APhysPolB.46.2501 [arXiv:1507.05267 [hep-ph]].

[107] A. Bacchetta, V. Bertone, C. Bissolotti, G. Bozzi, F. Delcarro, F. Piacenza and M. Radici, [arXiv:1912.07550 [hep-ph]].

[108] D. Boer, W. J. den Dunnen, C. Pisano, M. Schlegel and W. Vogelsang, Phys. Rev. Lett. **108** (2012), 032002 doi:10.1103/PhysRevLett.108.032002 [arXiv:1109.1444 [hep-ph]].

[109] F. Hautmann, H. Jung, M. Krämer, P. Mulders, E. Nocera, T. Rogers and A. Signori, Eur. Phys. J. C **74** (2014), 3220 doi:10.1140/epjc/s10052-014-3220-9 [arXiv:1408.3015 [hep-ph]].

[110] E. Blanco, A. van Hameren, H. Jung, A. Kusina and K. Kutak, Phys. Rev. D **100** (2019) no. 5, 054023, doi:10.1103/PhysRevD.100.054023 [arXiv:1905.07331 [hep-ph]].

[111] R. Loudon, *The Quantum Theory of Light*, Oxford University Press, New York, 2000.

[112] H.J. Metcalf and P. van der Straten, *Laser Cooling and Trapping*, Springer, New York, 1999.